Bioactive Materials 31 (2024) 333–354

Contents lists available at ScienceDirect

Bioactive Materials

journal homepage: www.keaipublishing.com/en/journals/bioactive-materials

Review article

Recent advances in Fe-based bioresorbable stents: Materials design and biosafety

Yang Zhang [a,c], Charles Roux [b], Aymeric Rouchaud [b], Anne Meddahi-Pellé [c], Virginie Gueguen [c], Claire Mangeney [a], Fan Sun [d,**], Graciela Pavon-Djavid [c,***], Yun Luo [a,*]

[a] Université Paris Cité, CNRS, Laboratoire de Chimie et de Biochimie Pharmacologiques et Toxicologiques, F-75006, Paris, France
[b] Univ. Limoges, CNRS, XLIM, UMR 7252, Limoges, France
[c] Université Sorbonne Paris Nord, INSERM U1148, Laboratory for Vascular Translational Science, Cardiovascular Bioengineering, 99 Av. Jean-Baptiste Clément, 93430, Villetaneuse, France
[d] PSL Université, Chimie Paris Tech, IRCP, CNRS UMR 8247, 11, Rue Pierre et Marie Curie, 75005, Paris, France

A B S T R A C T

Fe-based materials have received more and more interests in recent years as candidates to fabricate bioresorbable stents due to their appropriate mechanical properties and biocompatibility. However, the low degradation rate of Fe is a serious limitation for such application. To overcome this critical issue, many efforts have been devoted to accelerate the corrosion rate of Fe-based stents, through the structural and surface modification of Fe matrix. As stents are implantable devices, the released corrosion products (Fe^{2+} ions) in vessels may alter the metabolism, by generating reactive oxygen species (ROS), which might in turn impact the biosafety of Fe-based stents. These considerations emphasize the importance of combining knowledge in both materials and biological science for the development of efficient and safe Fe-based stents, although there are still only limited numbers of reviews regarding this interdisciplinary field. This review aims to provide a concise overview of the main strategies developed so far to design Fe-based stents with accelerated degradation, highlighting the fundamental mechanisms of corrosion and the methods to study them as well as the reported approaches to accelerate the corrosion rates. These approaches will be divided into four main sections, focusing on (i) increased active surface areas, (ii) tailored microstructures, (iii) creation of galvanic reactions (by alloying, ion implantation or surface coating of noble metals) and (iv) decreased local pH induced by degradable surface organic layers. Recent advances in the evaluation of the *in vitro* biocompatibility of the final materials and ongoing *in vivo* tests are also provided.

1. Introduction

Ischemic heart disease is the leading cause of death worldwide [1]. It accounted for 9,440,000 (8,820,000–9,960,000) deaths in 2021 [2]. Such a disease is mainly induced by narrowing (called stenosis) or occlusion of the arterial vessels. The common treatments are based on cardiovascular risk factors control and angioplasty by inserting and then inflating a tiny balloon temporarily, in order to widen the narrowed or obstructed arteries. It is often combined with the placement of a mesh tube, called stent, which helps prevent the artery from closing up again. However, a large number of patients suffer from restenosis after stent implantation. Recent studies suggested that in-stent restenosis could be due to the biological response (e.g. inflammation) triggered by the presence of the stent-based metallic platform injuring vascular wall [3]. To improve biocompatibility and prevent early restenosis, drug-eluting stents are currently used, because they are able to significantly induce an inhibition of neointimal proliferation. However, drug-eluting stents carry a higher thrombosis risk, mainly induced by delayed or absent endothelization of the stent struts, hypersensitivity, inflammatory and/or thrombotic adverse reactions [4].

Another promising approach is the use of bioresorbable stents (BRS), which avoid in-stent restenosis by self-degrading overtime. From the point of view of their physicochemical characteristics, the main requirements for bioresorbable stents are the preservation of their mechanical integrity for 3–6 months and their full degradation in 12–24 months [5]. In addition, the BRS must have biocompatibility and

Peer review under responsibility of KeAi Communications Co., Ltd.
* Corresponding author.
** Corresponding author.
*** Corresponding author.
E-mail addresses: yang.zhang@etu.u-paris.fr (Y. Zhang), charles.roux@aphp.fr (C. Roux), aymeric.rouchaud@unilim.fr (A. Rouchaud), anne.pelle@univ-paris13.fr (A. Meddahi-Pellé), virginie.gueguen@univ-paris13.fr (V. Gueguen), claire.mangeney@parisdescartes.fr (C. Mangeney), fan.sun@chimieparistech.psl.eu (F. Sun), graciela.pavon@univ-paris13.fr (G. Pavon-Djavid), yun.luo@u-paris.fr (Y. Luo).

https://doi.org/10.1016/j.bioactmat.2023.07.024
Received 24 April 2023; Received in revised form 27 July 2023; Accepted 27 July 2023

hemocompatibility properties allowing tissue regeneration and healing without inducing restenosis, thromboses or calcifications. However, the control of surface biocompatibility and degradation of bioresorbable stents still remains highly challenging, because few materials could fulfill both requirements. BRS based on biocompatible polymer of poly-L-lactide, has been commercialized and implanted in humans, but later withdrawn from sales due to the occurrence of restenosis effect similar to bare metal stents [6,7]. Besides, late shrinkage and non-uniform vessel support, induced by uneven degradation, was unveiled [7]. Mg alloys have been also explored as bioresorbable stents but they were degrading too fast. Indeed, within 4 months, the implanted Mg-based stents lost radial support due to reduced strut thickness, induced by surface erosion as the stent was absorbed [8]. Zn alloys demonstrate promising degradation rates and enhanced mechanical strength, largely due to alloying with elements such as Al, Li, Mg, Sr, Mn, and Ca [9–11], which allows for the creation of thin-strut stents comparable to modern stent-use CoCr alloys. Despite having different properties from strain-hardenable alloys traditionally used in stent and orthopedic devices, research is underway to balance strength and ductility in Zn alloys and adapt these properties for new stent design strategies. While chronic inflammation has been observed due to certain alloying elements [11], studies over the past five years affirm that Zn-based materials show potential for bioresorbable stents [9,12–16], albeit with considerable work needed for clinical application.

Fe and its alloys exhibit attractive mechanical properties, such as high strength, high elastic modulus, large ductility and important strain-hardening rate, combined with good biocompatibility, compared to Mg and Zn candidates. These advantages on mechanical properties enable thin strut design, low stent recoil and low risk of expansion fracture. A disadvantage of Fe stents is their slow degradation rate, as they remain virtually intact 53 months post-implantation [17], leading to prolonged retention times in the body. In order to improve the degradation rate, both metallurgical and surface strategies have been explored. The metallurgical approach to increase Fe degradation rate relies on two criteria which influence the corrosion susceptibility of the metal: (i) the addition of less noble alloying elements such as Mn within the solubility limit in Fe to make the Fe matrix more susceptible to corrosion [18]; and (ii) the addition of noble alloying elements to generate small and finely dispersed precipitates that act as cathodic sites towards the Fe matrix, inducing microgalvanic corrosion [19]. Another approach to increase Fe corrosion rate relies on surface coating by noble metals, such as Pt and Au microarrays [20,21], generating a multitude of galvanic cells on the surface. Recently, it was revealed that the biodegradation of Fe stents could be increased by surface coating of organic polylactide layers due to the decreased local pH induced by polylactide hydrolysis and alleviation of the passivation layer deposition [22]. As biosafety is the main concern in the development of new implantable devices, the biocompatibility of Fe-based BRS has been systematically evaluated *in vitro* and *in vivo*. The former includes direct- and indirect-contact (extracts and insert) tests using different cell lines, including animal ones such as mouse fibroblasts (3T3) or smooth muscle cell lines (VSMCs) and human cells in particular endothelial cells (HUVEC) [23]. The *in vivo* tests, carried out after the *in vitro* evaluation, are based on animal models such as rabbits, minipigs and juvenile domestic pigs and allow short or long term studies (from a few days to more than 4 years) [24]. As Fe-based materials attract more and more interests in the domain of BRS, a systematical review is necessary on the design, corrosion behavior and biosafety of such devices. Herein, we summarize and discuss the fundamental aspects of Fe-based BRS, including corrosion mechanism, materials design from material sciences point of view, *in vitro*, *in vivo* and clinical evaluations of Fe BRS.

2. Fundamentals aspects of Fe corrosion

Mechanism of Fe corrosion. The Fe corrosion is a redox reaction, summarized as an anodic reaction of Fe oxidation (**Equation (1)**) and a cathodic reaction of oxygen reduction (**Equation (2)**) in neutral or alkaline medium. For Fe implants, the pH value of the working conditions is 7.4 which corresponds to that of blood and that of most simulated body fluids (BSF) [25]. In BSF, the formed Fe^{2+} reacts with OH^-, generating $Fe(OH)_2$ (**Equation (3)**) which can be further oxidized to $Fe(OH)_3$ (**Equation (4)**). During formation of hydroxides, the deposition of calcium and phosphorus layers also takes place. The corrosion rate is thus reduced after several days due to surface coverage of these layers [26]. The thermodynamics and kinetics of Fe corrosion, represented by the corrosion potential and rate, exhibit variation depending on the type of bioresorbable Fe materials designed. The structure, surface and working environment have great impact. As described in section 3, one can tailor Fe microstructure (e.g. defects and grain), matrix porosity, composition (by integration of other elements) or surface chemistry (by polymer coating) to make Fe easier and faster to be corroded. The working environment can also affect corrosion kinetics. As reported by Mei *et al.*, for kinetic evaluation of a bioasorbable bare metal, increasing complexity of medium can lead to the decrease of corrosion rate [27]. For example, the corrosion rate might become lower in a medium containing various organic compounds and proteins, compared with a simple medium of inorganic ions [27]. However, if the material is optimized, the corrosion can be accelerated even in complex medium. For example, Fe corrosion became faster in presence of bovine serum albumin when the surface was coated by a thin layer of polyethyleneimine due to interaction of protein with polymer coating [28]. Therefore, it is important to investigate the corrosion rate during *in vitro* and *in vivo* environment. These aspects are introduced and summarized in section 4.

$$Fe \rightarrow Fe^{2+} + 2e^- \quad (1)$$

$$O_2 + H_2O + 4e^- \rightarrow 4OH^- \quad (2)$$

$$Fe^{2+} + 2OH^- \rightarrow Fe(OH)_2 \quad (3)$$

$$4Fe(OH)_2 + O_2 + 2H_2O \rightarrow 4Fe(OH)_3 \quad (4)$$

In the human body, the anodic reaction, namely, oxidation of Fe (**Equation (1)**) remains the same but the products participate in metabolism and undergo Fenton reaction that generates radicals [29–32]. In aerobic condition, Fe^{2+} reacts with oxygen and forms superoxide anion (**Equation (5)**), followed by H_2O_2 generation (**Equation (6)**). The interaction of H_2O_2 and Fe^{2+} products hydroxyl radical (**Equation (7)**), known as Fenton reaction [29–32], inducing oxidative stress [23].

$$Fe^{2+} + O_2 \rightarrow Fe^{3+} + O_2^{\bullet-} \quad (5)$$

$$Fe^{2+} + O_2^{\bullet-} + 2H^+ \rightarrow Fe^{3+} + H_2O_2 \quad (6)$$

$$Fe^{2+} + H_2O_2 \rightarrow Fe^{3+} + OH^{\bullet} + OH^- \quad (7)$$

Therefore, for Fe-based BRS, the control of reactive oxygen species (ROS), here $OH^{\bullet}$ releasing and the improvement of biocompatibility is very important. The impact of such an effect toward biological process and biosafety will be discussed in detail in section 4.

Determination of Fe corrosion rate. The most common methods to evaluate corrosion rate (CR) are electrochemical and immersion test, as suggested by ASTM-G102-89 [33] and ASTM-G31-72 [34] standard protocols. The former provides corrosion information under controlled potential or/and current while the later without. Electrochemical measurements (operated in a three-electrodes system and controlled by a potentiostat), including potentiodynamic polarization and electrochemical impedance spectroscopy (EIS), are the most widely employed tests for fast evaluation of corrosion properties. The information obtained from electrochemical measurements are rich (such as open cycle potential, corrosion potential/current, resistance/capacitance, etc.), providing insights on corrosion mechanisms. The CR value can be calculated through analysis of the Tafel plot derived from the potentiodynamic polarization curve, using **Equation (8)** [35].

$$CR = 3.72 \times 10^{-3} \times i_{corr} \times EW / \rho \quad (8)$$

Where the i_{corr} is corrosion current density (A cm^{-2}) derived from Tafel plot, EW the equivalent weight of iron (27.92 g/eq) and ρ the material density in grams per cubic centimeter (7.87 for Fe). The immersion test aims to estimate CR value by the weight loss of samples via **Equation (9)**.

$$CR = m / (S \times t) \quad (9)$$

Where m is the sample weight loss which can be directly weighted or calculated from released ion concentration, S surface area of sample and t immersion time. The static immersion test (ASTM-G31-72) is conducted by immersing the specimen into the bath at 37 °C. After n days (usually, n varies from 3 to 180 days), samples are removed from the bath, followed by washing and drying, for weighting. In addition, dynamic immersion tests can be also employed to evaluate CR [36]. Such a setup is designed to simulate blood flow in the coronary artery. The specimen is immersed into a fluidic system where the flow speed, sample wall shear stress, dissolved oxygen level and pH value are controlled.

Many factors affect the corrosion test results. For example, to obtain an accurate potentiodynamic polarization curve, the scan rate should not be too fast, usually at 0.166 mV s^{-1} [35,37] and 0.33 mV s^{-1} in literatures [21,38], but could be extended to 0.5 or 1 mV s^{-1} [26,39,40]. Higher total current density can be observed with increasing scan rate. In EIS, the frequency, generally ranging in 100 kHz - 10 mHz [41,42], should be adapted to the stability of the sample or to avoid sample surface deterioration in electrolyte and to reduce noises. For immersion tests, the ratio of solution volume to sample surface area is crucial [43], which should be 20 or 40 mL cm^{-2} as suggested by ASTM-G31-72. But the international standard organization (ISO10993-15) suggested keeping the ratio lower than 1 mL cm^{-2}. In any case, the immersion solution volume should be adapted to sample oxidation properties, avoiding oxygen exhaustion and surface accumulation of corrosion products. In addition, immersion solution type has also an impact. It seems that the corrosion rate is lower in a medium containing complex components with respect to simple medium [27]. For example, the corrosion is decreased in a cell culture medium (that contains inorganic ions, organic compounds and proteins) with respect to that in NaCl solution [27]. For dynamic immersion tests, the flow rate simulating blood in the human body is set to 40 mL min^{-1} [44]. For Fe-based BRS, as reported by *Liu* et al., the wall shear stress (0.68 Pa), dissolved oxygen (2.8–3.2 mg L^{-1}) and pH (7.34–7.45) should be considered as experimental parameters [36]. The CR value of a sample obtained by electrochemical measurement should display the same trend to that from static or dynamic immersion tests.

Characterization for fundamental studying of Fe corrosion. Surface and structure characterizations before and after corrosion tests are essential and necessary for fundamental studying of Fe corrosion and understanding the reaction mechanism. As shown in Fig. 1, the topographic or structural images with surface chemistry (composition, bonding and energy) should be collected and investigated to understand the corrosion behavior. Scanning electron microscopy (SEM) coupled with energy-dispersive X-ray spectroscopy (EDS) has been widely applied for this purpose. This technique provides information on structure, surface morphology and composition. For example, porous Fe, with high surface roughness and high concentration of dislocations sites, have been

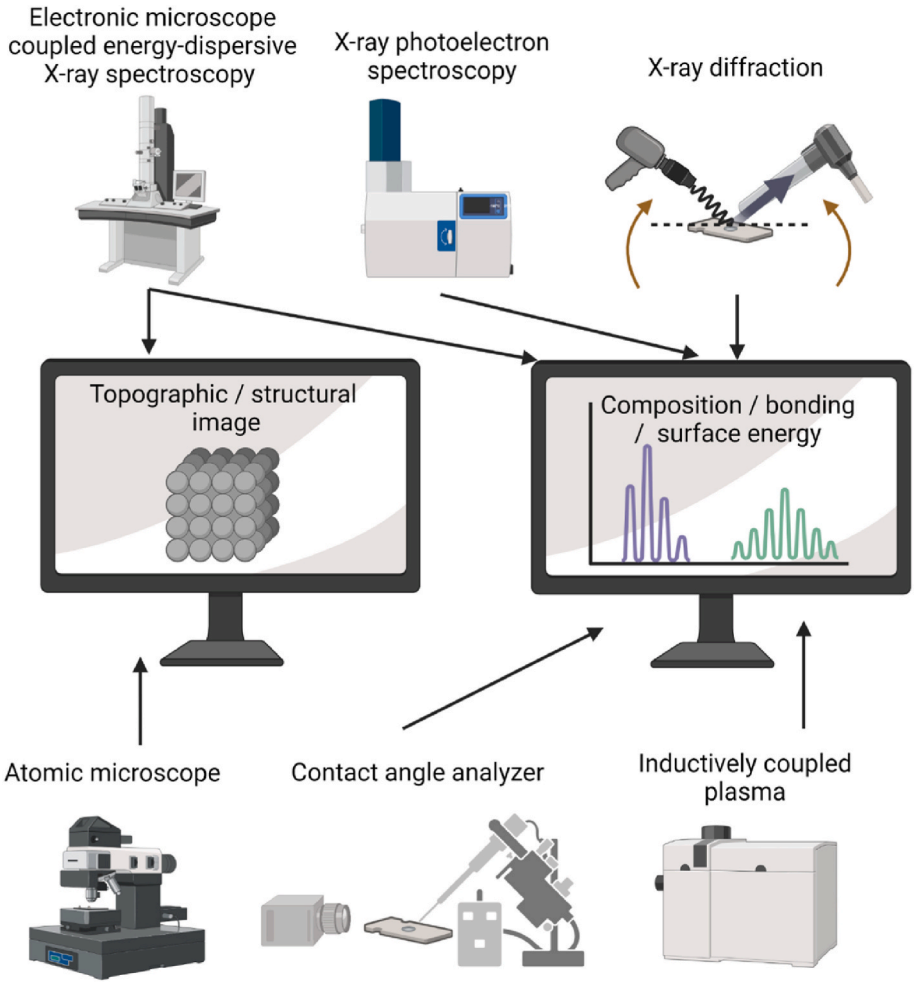

Fig. 1. The illustrative scheme of equipments for surface and structure analysis in the domain of Fe-based BRS. Created with Biorender.

fabricated to serve as BRS due to the accelerated CR [39]. As revealed by SEM images, the porous morphology of Fe scaffold can be confirmed. Another example is Ta-implanted Fe surface [45]. Such a material has been characterized by SEM-EDS, confirming the formation of surface nanoridges covered by Ta on Fe substrate. After corrosion tests, the specimen can be also analyzed by SEM-EDS, investigating surface topography (e.g. pitting or cracking) [45] and chemistry (e.g. corrosion products, passivation layer deposition) [46]. X-ray photoelectron spectroscopy (XPS) is also used for surface chemistry analysis. One example is Fe–Mn alloy that has been reported for improved biodegradation [47]. Using SEM and XPS, the topography and the formation of Fe and Mn oxides on the surface after laser ablation should be associated with increased degradation. In addition, X-ray diffraction (XRD), delivering crystalline structural information, has been applied to characterize surface components. For example, using XRD, one can verify the formation of alloy or oxide coating [42,48]. Atomic force microscopy (AFM) can also provide surface morphology, such as roughness [49]. Contact angle analyzer has been used for hydrophilicity of surface [50]. Inductively coupled plasma (ICP) could provide released iron concentration after corrosion tests [42]. Nowadays, Raman spectroscopy has emerged as an interesting surface analysis technique for developing BRS by offering a comprehensive understanding of surface composition and bonding information. Additionally, this method enables the generation of images with both spectral and spatial information, further enhancing its capabilities for surface characterization. It thus proved particularly useful in investigating the corrosion behavior of materials made of iron (Fe), offering valuable data for further analysis and understanding of the corrosion process/products [28].

3. Strategy to accelerate Fe corrosion

Various approaches can be employed to improve corrosion rate, as illustrated in Fig. 2.

(i) Increasing Fe active surface area by enhancing roughness and porosity. Increased Fe surface roughness or porosity leads to increased electrochemical active surface area, inducing improved corrosion rates [39].
(ii) Creating fine grained microstructure with higher volume of grain boundaries. This leads to an increased number of active sites, thereby increasing the susceptibility of corrosion attack [41].
(iii) Alloying or ion implantation. Fe corrosion can be accelerated by introducing second phases into the matrix, e.g. Fe–Mn, Fe–W alloys [44,47]. Besides, surface ions implantation (such as Zn) has been reported for accelerated Fe corrosion [49].
(iv) Surface coating of inorganic and organic layer. It could be a coating of an inorganic galvanic layer, with higher oxidation potential (such as Ta, Au, Pt, carbon, etc.) [20,21,45]; or, through organic coating to decrease local pH (e.g. polylactide), hydrolysis or/and inhabitation of the deposit of passivation layer during corrosion can be also employed to increase CR [22,51].

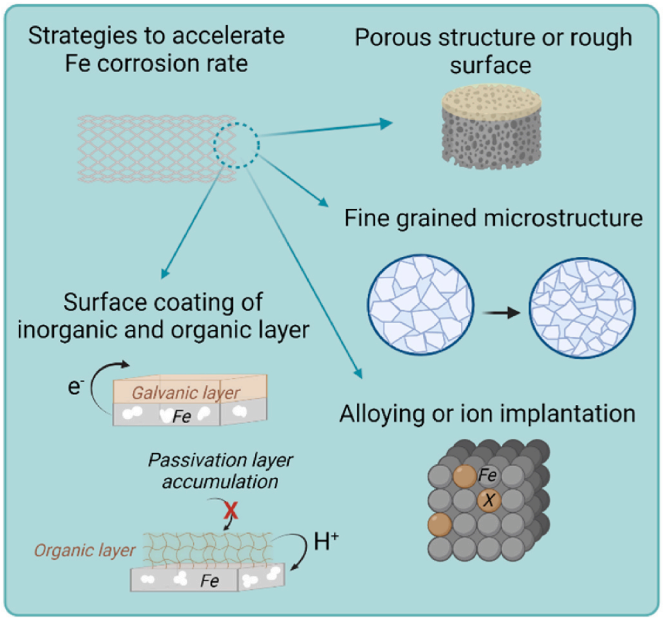

Fig. 2. Illustrative scheme of the strategies to accelerate iron corrosion via (i) increasing surface porosity and roughness; (ii) Creating fine grained microstructure; (iii) alloying or ion implantation; and (iv) surface coating of microgalvanic layer or polymer to decrease local pH or/and inhabit of passivation layer deposition. Created with Biorender.

Approaches (i) and (ii) are respectively surface and structure strategies which are mainly used to accelerate corrosion of pure Fe stents; these two methods will be introduced in section 3.1. Methods (iii) and (iv) developed for bioresorbable stents on Fe-based alloys or composites, will be summarized in section 3.2 and section 3.3, respectively.

3.1. Increasing corrosion rate of pure fe

Tunable Fe surface morphology or/and microstructure engineering can increase the mechanical properties and corrosion rate by properly inducing porous structure, microstructural defects and grain refinement.

Porous Fe structure. *Wegener* et al. recently reported porous Fe implants fabricated by powder sintering technique. The animal test results demonstrated that the degradation of the implant was detected, and the porous Fe-based material is a promising candidate for self-degrading and high load bearing implant material [52]. In order to understand the influences of porous structure to corrosion rate, *P. Sharma* et al. have compared porous Fe scaffold samples having random microporous structure and topologically ordered porous structure (as shown in Fig. 3a) [39]. The manufacturing of the porous structures employed prefabricated moulds with different pore topologies to sinter Fe powder in the mould [53]. The potentiodynamic assessment results showed that the increase in random microporosity leads to higher corrosion susceptibility (Fig. 3b). As listed in Table 1, the corrosion potential was more negatively shifted on random porous Fe with the highest porosity (39.60 %) with highest corrosion current, with respect to less random porous samples (16.83 % and 29.80 % of porosity). And the reduction of the macropore (strut) size resulted in the same effect up to 2.5 times higher on corrosion rate (Fig. 3c, cf. CR value of topological ordered porous Fe samples in Table 1). The highest corrosion rate was recorded on topologically ordered porous iron scaffold (with 1 mm strut size), it was found about 17 times higher than that of non-porous Fe sample (Table 1). Similar results have been reported by *N. E. Putra* et al. [46] who showed that the presence of geometrically designed macropores and random micropores improved the *in vitro* corrosion rate of the scaffold as compared to the bulk counterpart. The porous Fe presented 7 % of mass loss after 28 days' immersion test. It is worthy to note that the CR value from immersion test was 2.8 g m^{-2} day^{-1} at day 1, but declined to 1.1 g m^{-2} day^{-1} at day 28, probably due to surface accumulation of corrosion products (Table 1). Such a value (at day 28) is much higher than cast pure iron or porous iron in literatures (0.4–0.8 g m^{-2} day^{-1}) [44,50,54]. The acceleration of degradation rate was also observed in the study in which topologically ordered porous structure was achieved by direct metal printing technique [40]. The electrochemical tests showed up to about 12 times higher rates of corrosion for this porous Fe sample (1.18 mm $year^{-1}$) as compared to that of bulk Fe (0.1 mm $year^{-1}$), see Table 1.

The reason for the accelerated CR on porous structure can be attributed to the increased specific surface area which is in direct contact with the electrolyte. Since the porous material is less dense than the bulk

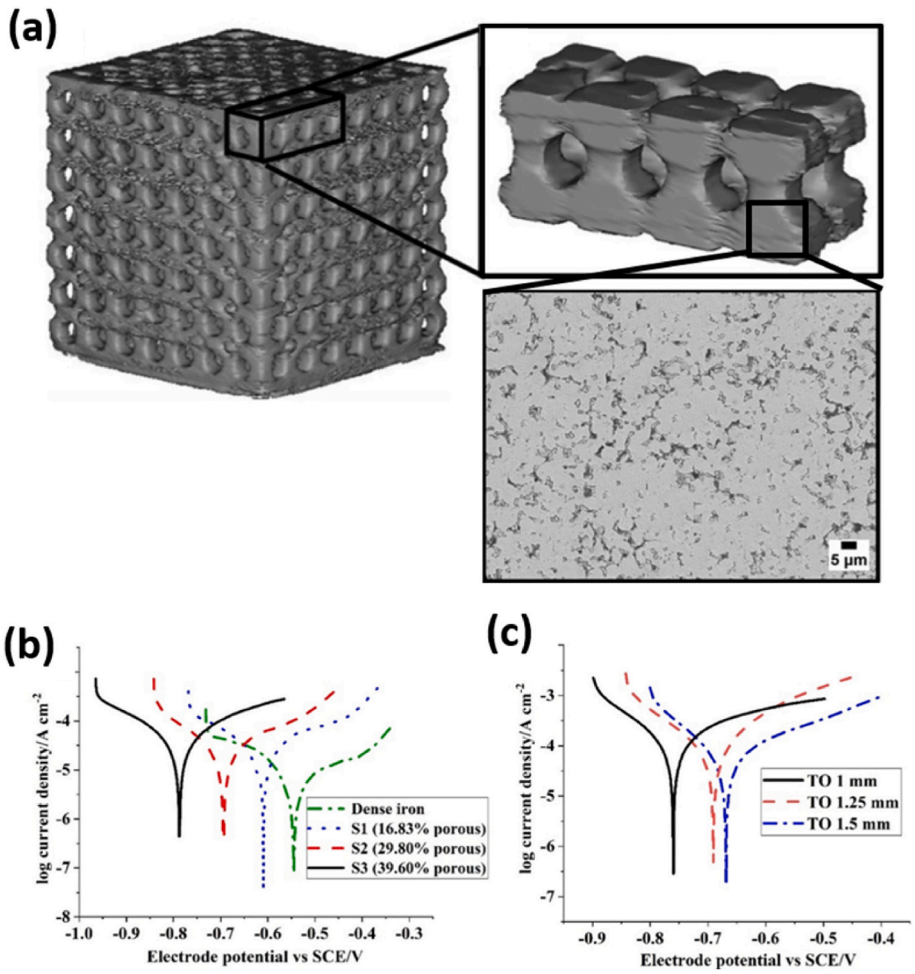

Fig. 3. (A) Construction of 3D macroporous Fe structure from computerized tomography (CT) scan and SEM picture of microporous sample surface. Comparison of potentio-dynamic polarization curves for (b) dense and microporous Fe sample (S1–S3), (c) macroporous samples (TO) with different strut size. Adapted from Ref. [39], copyright 2019, Elsevier.

one, for implants of the same size, the one made by porous material presents less mass to be degraded. Moreover, the corrosion rate, characterized by mass loss per unit surface area per duration, is also increased by porous structure which accelerates the degradation process in addition to the two above advantages. The mechanism has been suggested that the microporous structure resulted in intricate paths which were conducive to corrosion [39]. As a confinement effect in crevice corrosion, these paths slow the movement of corrosion species resulting in a local rise of acidity. It is also suggested that the reason could be attributed to the occurrence of an autocatalytic process in the micropores as an anode, and the cathodic reduction reaction occurred on Fe scaffold surface outside the micropores. Thus, to maintain the charge neutrality, the Cl^- ions from the electrolyte were attracted inside the micropores, thereby resulting in the rapid dissolution of Fe. For bioresorbable application in cardiovascular implants, for instance the vascular stent, porous Fe shows advantages on dissolution rate regulation and important potential on drug-carrying and eluting. However, the challenges on mechanical properties, such as ductility and fatigue resistance, present in the stent expansion process and the maintenance of structural integrity during the artery healing process where radial support is indispensable. In numerous studies documented in Tables 1 and it has been consistently found that both tensile and compressive stresses are significantly lower in porous Fe compared to its bulk pure form. For porous Fe, the tensile yield stresses fluctuate within the range of 7.2–27.8 MPa. This is markedly below the tensile yield stress exhibited by bulk Fe, which is around 140 MPa. Typically, a decrease in mechanical strength necessitates an increase in implant size to ensure sufficient supportive force. Nevertheless, this poses a challenging dynamic as the dimensions of implants, such as the strut thickness in cardiovascular stents, significantly impact both the healing process and long-term clinical outcomes. Take modern coronary stents as an example, their thickness can be as little as 75 μm, a feature designed to optimize clinical outcomes. However, this necessitates an alloy tensile strength exceeding 400 MPa. The balance between the porous structure of the implant and its mechanical properties becomes an intricate problem in biomedical engineering.

Surface/structural grain refinement can be achieved via mechanical deformation method such as shot peening technique. The technique uses small spherical particles of high hardness striking the material surface at high velocity in order to create dimple-like local plastic deformation sites. The overlapping dimples form a continuous surface layer with high residual stress and high density of dislocations. The original grain structure of the alloy can therefore be refined to a level depending on the time and energy of the peening process. *Bagherifard* et al. have achieved accelerated corrosion and improved mechanical performance of pure iron through surface grain refinement [41]. They reported that severe shot peening could notably increase the surface roughness and grain refinement. The surface hardness has been largely increased due to the high density of dislocations and compressive residual stresses. It also showed that high concentration of micro cracks was observed on the top

Table 1
The mechanical and degradation properties of Fe-based materials.

Ref.	Sample	Mechanical properties			Degradation properties			
		Ultimate tensile stress/MPa	Tensile yield stress/MPa	Compressive yield stress/MPa	E_{corr}/V	J_{corr}/μA cm^{-2}	CR[a]/mm $year^{-1}$	CR[b] (immersion time)/g m^{-2} d^{-1}
Porous Fe								
[39]	Dense Fe (reference sample)	N.A.	N.A.	N.A.	−0.545 vs. SCE	11.53	0.13	N.A.
	Random Porous Fe (16.83 % porosity)	N.A.	N.A.	N.A.	−0.609 vs. SCE	42.96	0.50	N.A.
	Random Porous Fe (29.80 % porosity)	N.A.	N.A.	N.A.	−0.694 vs. SCE	65.51	0.76	N.A.
	Random Porous Fe (39.60 % porosity)	N.A.	N.A.	N.A.	−0.738 vs. SCE	83.97	0.98	N.A.
	Topological ordered porous Fe (1 mm strut size, 45.63 % porosity)	N.A.	N.A.	N.A.	−0.760 vs. SCE	193.34	2.25	N.A.
	Topological ordered porous Fe (1.25 mm strut size, 59.99 % porosity)	N.A.	N.A.	N.A.	−0.691 vs. SCE	115.87	1.35	N.A.
	Topological ordered porous Fe (1.5 mm strut size, 80.97 % porosity)	N.A.	N.A.	N.A.	−0.669 vs. SCE	73.34	0.85	N.A.
[46]	Porous Fe	N.A.	7.2 (day 1) 9.4 (day 28)	96 (day 1) 19 (day 28)	−0.781 vs. Ag/AgCl (day 1) −0.676 vs. Ag/AgCl (day 28)	8.0 (day 1) 3.5 (day 28)	0.09 (day 1) 0.04 (day 28)	2.8 (day 1) 1.1 (day 28)
[40]	Cold-rolled Fe (reference sample)	N.A.	N.A.	N.A.	N.A.	8.6 (day 1)	0.10 (day 1)	N.A.
	Porous Fe	N.A.	27.8 (day 1) 22.4 (day 28)	N.A.	N.A.	102.8 (day 1)	1.18 (day 1)	N.A.
Fine-grain Fe								
[35]	Pure Fe, annealed at 550 °C (reference sample)	205	140	N.A.	−0.732 vs. SCE	14	0.16	N.A.
	E-Fe, annealed at 550 °C	292	270	N.A.	−0.776 vs. SCE	44.3	0.51	N.A.
	E-Fe	423	360	N.A.	−0.824 vs. SCE	73.4	0.85	N.A.
[58]	Annealed Fe at 1100 °C	274	104	N.A.	Between −0.55 and −0.6 V vs. SCE	N.A.	0.099[c]	1.2 (day 1)[e] 1.3 (day 7)[e]
	Annealed Fe at 1200 °C	275	137	N.A.	Between −0.55 and −0.6 V vs. SCE	N.A.	0.101[c]	3.0 (day 1)[e] 2.6 (day 7)[e]
	Annealed Fe at 1300 °C	279	139	N.A.	Between −0.55 and −0.6 V vs. SCE	N.A.	0.100[c]	4.5 (day 1)[e] 2.6 (day 7)[e]
	As-sprayed Fe	84	N.A.	N.A.	−0.70 vs. SCE	N.A.	0.097[c]	6.5 (day 1)[e] 3.8 (day 7)[e]
Alloyed Fe								
[61]	Fe	N.A.	N.A.	N.A.	−0.236 vs. SCE	4.67	N.A.	N.A.
	$Fe_{87}Mg_9Zn_4$	N.A.	N.A.	N.A.	−0.305 vs. SCE	3.97	N.A.	N.A.
	$Fe_{74}Mg_{19}Zn_7$	N.A.	N.A.	N.A.	−0.773 vs. SCE	7.87	N.A.	N.A.
	$Fe_{60}Mg_{30}Zn_{10}$	N.A.	N.A.	N.A.	−0.832 vs. SCE	9.72	N.A.	N.A.
[63]	Fe (reference sample)	N.A.	N.A.	N.A.	−0.594 vs. Ag/AgCl	3.3	0.04	1.296 (day 30)[d]
	$Fe_{65}Mn_{35}$	N.A.	N.A.	N.A.	−0.747 vs. Ag/AgCl	34.0	0.51	6.695 (day 30)[d]
	$Fe_{65}Mn_{35}Ag_1$	N.A.	N.A.	N.A.	−0.764 vs. Ag/AgCl	57.8	0.96	19.01 (day 30)[d]
[47]	Fe (reference sample)	N.A.	N.A.	N.A.	−0.735 vs. SCE	N.A.	$6.2 \cdot 10^{-5}$	N.A.
	Polished Fe–Mn	N.A.	N.A.	N.A.	−0.699 vs. SCE	N.A.	$1.21 \cdot 10^{-4}$	N.A.
	Laser-textured Fe–Mn	N.A.	N.A.	N.A.	−0.755 vs. SCE	N.A.	$8.63 \cdot 10^{-4}$	N.A.
[64]	Fe–30Mn (reference sample)	N.A.	N.A.	N.A.	−0.725	11.62	0.127	1.08 (day 30)[d]
	Fe–30Mn prepared by continuous laser	N.A.	N.A.	N.A.	−0.776	10.85	0.114	1.01 (day 30)[d]
	Fe–30Mn prepared by nanosecond laser	N.A.	N.A.	N.A.	−0.596	18.54	0.136	1.27 (day 30)[d]
	Fe–30Mn prepared by femtosecond laser	N.A.	N.A.	N.A.	−0.903	69.22	0.179	1.51 (day 30)[d]
[50]	Pure Fe	N.A.	148	N.A.	−0.324 vs. SCE	0.871	N.A.	0.44 (Static, day 30)[e] 0.63 (dynamic, day 30)[e]
	Fe–Pd	N.A.	445	754	−0.471 vs. SCE	1.550	N.A.	0.74 (Static, day 30)[e] 1.63 (dynamic, day 30)[e]
	Fe–Pt	N.A.	503	785	−0.545 vs. SCE	6.698	N.A.	1.21 (Static, day 30)[e] 1.88 (dynamic, day 30)[e]
[48]	As-cast pure iron (reference sample)	N.A.	140[e]	N.A.	−0.727 vs. SCE	3.742	0.043	0.62 (Static, day 30)[e]

(*continued on next page*)

Table 1 (*continued*)

Ref.	Sample	Mechanical properties			Degradation properties			
		Ultimate tensile stress/MPa	Tensile yield stress/MPa	Compressive yield stress/MPa	E_{corr}/V	J_{corr}/μA cm^{-2}	CR[a]/mm $year^{-1}$	CR[b] (immersion time)/g m^{-2} d^{-1}
								1.40 (dynamic, day 30)[e]
	As-sintered pure ion (reference sample)	N.A.	250[e]	N.A.	−0.860 vs. SCE	6.018	0.071	0.70(Static, day 30)[e]
								1.59 (dynamic, day 30)[e]
	Fe–2Ag	N.A.	210[e]	N.A.	−0.841vs. SCE	10.19	0.120	0.72 (Static, day 30)[e]
								1.74 (dynamic, day 30)[e]
	Fe–5Ag	N.A.	380[e]	N.A.	−0.856 vs. SCE	12.17	0.140	0.90 (Static, day 30)[e]
								2.06 (dynamic, day 30)[e]
	Fe–10 Ag	N.A.	200[e]	N.A.	−0.891 vs. SCE	15.19	0.175	0.78 (Static, day 30)[e]
								1.87 (dynamic, day 30)[e]
	Fe–2Au	N.A.	350[e]	N.A.	−0.809 vs. SCE	14.97	0.174	0.73 (Static, day 30)[e]
								1.73 (dynamic, day 30)[e]
	Fe–5Au	N.A.	250[e]	N.A.	−0.796 vs. SCE	11.50	0.131	0.98 (Static, day 30)[e]
								2.31 (dynamic, day 30)[e]
	Fe–10Au	N.A.	350[e]	N.A.	−0.779 vs. SCE	8.833	0.098	0.87 (Static, day 30)[e]
								1.72 (dynamic, day 30)[e]
[60]	*M*-Fe	N.A.	N.A.	N.A.	−0.673 vs. SCE	5.84	0.137	2.57[d]
	E-Fe	N.A.	N.A.	N.A.	−0.701 vs. SCE	5.93	0.139	3.48[d]
	Fe–Zn (7.2 wt%)	N.A.	N.A.	N.A.	−0.798 vs. SCE	9.85	0.231	5.31[d]
	Fe–Zn (4.6 wt%)	N.A.	N.A.	N.A.	−0.818 vs. SCE	13.76	0.323	5.77[d]
	Fe–Zn (2.1 wt%)	N.A.	N.A.	N.A.	−0.761 vs. SCE	10.15	0.238	4.56[d]
	Fe–Zn (2.3 wt%)	N.A.	N.A.	N.A.	−0.857 vs. SCE	7.68	0.180	13.6[d]
[19]	solution- heat- treated low carbon steel (reference sample)	900	700	N.A.	N.A.	N.A.	N.A.	0.86 (day 1)[e]
								0.58 (day 2)[e]
	Fe–10Mn with heat treatments (reference sample)	1300	650	N.A.	N.A.	N.A.	N.A.	3.97 (day 1)[e]
								2.50 (day 2)[e]
	Fe–10Mn–1Pt with heat treatments	1450	850	N.A.	N.A.	N.A.	N.A.	6.68 (day 1)[e]
								9.05 (day 2)[e]
[66]	Fe	N.A.	N.A.	320	−0.97 vs. SCE	0.58	0.007	N.A.
	Fe–30Mn	N.A.	N.A.	94	−1.11 vs. SCE	0.60	0.007	N.A.
	Fe–30Mn–Ag	N.A.	N.A.	130	−1.10 vs. SCE	0.89	0.012	N.A.
[62]	Fe	N.A.	N.A.	N.A.	−0.533 vs. SCE	6.21	0.078[e]	1.84 (day 28)[d,e]
	Fe/0.3CNTs	N.A.	N.A.	N.A.	−0.595 vs. SCE	7.28	0.090[e]	2.05 (day 28)[d,e]
	Fe/0.6CNTs	N.A.	N.A.	N.A.	−0.628 vs. SCE	12.83	0.160[e]	2.27 (day 28)[d,e]
	Fe/0.9CNTs	N.A.	N.A.	N.A.	−0.683 vs. SCE	17.55	0.225[e]	3.20 (day 28)[d,e]
	Fe/1.2CNTs	N.A.	N.A.	N.A.	−0.712 vs. SCE	19.95	0.241[e]	3.30 (day 28)[d,e]
Ion implanted Fe								
[68]	Pure Fe (reference sample)	N.A.	N.A.	N.A.	−0.582 vs. SCE	2.340	0.027[c]	0.09 (day 3)[e]
								0.49 (day 15)[e]
								0.48 (day 30)
	Zn-implanted Fe	N.A.	N.A.	N.A.	−0.901 vs. SCE	8.001	0.098[c]	0.35 (day 3)[e]
								0.68 (day 15)[e]
								0.60 (day 30)
[49]	Fe (reference sample)	N.A.	N.A.	N.A.	−0.648 vs. SCE	2.19	N.A.	N.A.
	Zn–Fe-5	N.A.	N.A.	N.A.	−0.722 vs. SCE	26.07	N.A.	N.A.
	Zn–Fe-10	N.A.	N.A.	N.A.	−0.727 vs. SCE	21.07	N.A.	N.A.
	Zn–Fe-40	N.A.	N.A.	N.A.	−0.713 vs. SCE	2.01	N.A.	N.A.
[45]	Fe (reference sample)	180 (week 0)[e]	N.A.	N.A.	−0.728 vs. SCE	4.920	0.057	N.A.
		148 (week 12)[e]						
		122 (week 40)[e]						
	Nano Ta–Fe	176 (week 0)[e]	N.A.	N.A.	−0.754 vs. SCE	13.836	0.161	N.A.
		170 (week 12)[e]						
		177 (week 40)[e]						
Fe with inorganic surface coating								
[21]	Pure Fe (reference sample)	N.A.	N.A.	N.A.	−0.699 vs. SCE	9.642	0.112	1.485 (day 42)
	Fe with Pt disc arrays (Φ20 μm × S5 μm)	N.A.	N.A.	N.A.	−0.763 vs. SCE	17.698	0.206	3.456 (day 42)
	Fe with Pt disc arrays (Φ4 μm × S4 μm)	N.A.	N.A.	N.A.	−0.886 vs. SCE	19.754	0.223	3.824 (day 42)

(*continued on next page*)

Table 1 (*continued*)

Ref.	Sample	Mechanical properties			Degradation properties			
		Ultimate tensile stress/MPa	Tensile yield stress/MPa	Compressive yield stress/MPa	E_{corr}/V	J_{corr}/μA cm^{-2}	CR[a]/mm $year^{-1}$	CR[b] (immersion time)/g m^{-2} d^{-1}
[20]	Pure Fe (reference sample)	N.A.	N.A.	N.A.	−0.579 vs. SCE	2.461	0.029	0.917 (day 30)
	Fe with 200 × 200 μm^2 Au disc	N.A.	N.A.	N.A.	−0.627 vs. SCE	9.325	0.108	1.184 (day 30)
	Fe with 50 × 50 μm^2 Au disc	N.A.	N.A.	N.A.	−0.575 vs. SCE	12.66	0.147	1.134 (day 30)
	Fe with (fully coated) 0 × 0 μm^2 Au disc	N.A.	N.A.	N.A.	−0.665 vs. SCE	10.71	0.124	1.417 (day 30)
Fe with organic surface coating								
[69]	Porous Fe (reference sample)	N.A.	0.22	0.28	−0.71 vs. Ag/AgCl	2.33	0.11	7.127 (week 4)[d]
	PLGA coated porous Fe	N.A.	0.65	0.71	−0.73 vs. Ag/AgCl	5.18	0.42	16.41 (week 4)[d]
	PLGA infiltrated porous Fe	N.A.	0.38	0.42	−0.78 vs. Ag/AgCl	9.84	0.72	138.7 (week 4)[d]
[51]	Bare Fe (reference sample)	N.A.	N.A.	N.A.	−0.50 vs. SCE (day 0)[e] −0.80 vs. SCE (day 5)[e] −0.79 vs. SCE (day 10)[e] −0.84 vs. SCE (day 28)[e]	8.2 (day 0)[e] 3.5 (day 5)[e] 3.0 (day 10)[e] 2.5 (day 28)[e]	N.A.	N.A.
	PMMA-coated Fe (reference sample)	N.A.	N.A.	N.A.	−0.36 vs. SCE (day 0)[e] −0.87 vs. SCE (day 5)[e] −0.96 vs. SCE (day 10)[e] −0.94 vs. SCE (day 28)[e]	2.1 (day 0)[e] 1.0 (day 5)[e] 2.0 (day 10)[e] 2.7 (day 28)[e]	N.A.	N.A.
	PLA-coated Fe (reference sample)	N.A.	N.A.	N.A.	−0.51 vs. SCE (day 0)[e] −0.93 vs. SCE (day 5)[e] −0.94 vs. SCE (day 10)[e] −0.98 vs. SCE (day 28)[e]	8.2 (day 0)[e] 10.3 (day 5)[e] 11.0 (day 10)[e] 14.0 (day 28)[e]	N.A.	N.A.

TS = tensile strength; YS = yield strength; CS = ultimate compressive strength; E_{corr} = corrosion potential; J_{corr} = corrosion current density; SCE = saturated calomel electrode.

N.A. = not analyzed.

[a] Data from electrochemical test

[b] Data from immersion test.

[c] Data converted from g m^{-2} day^{-1} (= 0.0463 mm $year^{-1}$).

[d] Data converted from mm $year^{-1}$ (= 21.6 g m^{-2} day^{-1}).

[e] Data estimated from figures.

layer. The cracks are considered favorable to promote pure iron's degradation. But their influences to the mechanical properties were not evaluated.

The fine-grain Fe thin foil can be formed by electrochemical deposition of pure Fe onto a metallic substrate in ferrous chloride–calcium chloride aqueous solution. *Moravej* et al. has characterized the corrosion rate, mechanical properties and microstructure of pure Fe foil by electroforming technique [35]. Equiaxial fine grains at 4 μm in size with strong (111) fiber texture was found in the *as*-electroformed sample (*E*-Fe). The ultimate tensile stress and tensile yield stress witnessed a remarkable increase, reaching respective values of 432 MPa and 360 MPa. When compared to pure Fe, which has an ultimate tensile stress of 205 MPa and a tensile yield stress of 140 MPa, the *E*-Fe sample exhibits a significantly enhanced mechanical strength. This improved strength shows great potential for stent design, enabling the creation of thin-strut stents comparable in thickness to modern versions (approximately 75 μm) as previously mentioned. In this state, the corrosion potential was negatively shifted of 110 mV; and corrosion current density was ca. 5-foder higher, with respect to pure Fe. The corrosion rate was increased (0.85 g m^{-2} day^{-1}) over 5 times due to the high internal stress and electroforming defects when compared to conventional pure Fe samples (0.16 g m^{-2} day^{-1}, data summarized in Table 1). After being annealed to retain ductility, the corrosion rate was considerably reduced to 0.51 g m^{-2} day^{-1} because of the grain growth and the elimination of internal stress and structural defects. The ultimate tensile stress and tensile yield stress were found to decrease to 292 MPa and 270 MPa respectively, which points to a reduction in the alloy's strength as a result of thermal treatments performed at 550 °C. At this particular temperature, the material experiences recovery and likely partial recrystallization. These processes contribute to a decrease in dislocation density, defects, and internal stress. Generally, it's worth noting that, aside from the *E*-Fe sample, Fe after annealing with lower refinement defects or internal stress can demonstrate enhanced ductility. However, this comes at the cost of reduced corrosion rate and mechanical strength, leading to a delicate equilibrium between strength and ductility.

One should notice that the grain refinement mentioned in these literature [35,41] has shown that grain size reduction with structural defects due to the processes. The defects, including dislocations and surface cracks, and internal stress are key outcomes of the mechanical grain refinement, serves as a potent promoter for augmenting corrosion rates. However, in the recrystallized pure Fe, it has been shown proportional relationship between grain size and corrosion rate due to the removal of refinement induced defects, as reported in Ref. [55]. Therefore, after thermal treatment such as recrystallization, pure Fe with finer grain without refinement defects or internal stress can show reduction of corrosion rate when comparing to larger grains.

Techniques such as Equal-Channel Angular Pressing (ECAP) and High Pressure Torsion (HPT), used for causing severe plastic deformations, can dramatically refine the grain structure and lead to a significant density of structural defects. The intricate details of these

techniques are reviewed in the referenced article [56]. It's worth highlighting the research on Fe–Mn–C alloys, which, after ECAP, exhibited the development of an ultrafine-grained structure [57]. This refinement enhanced the alloys' strength without compromising their biocompatibility. The corrosion rate was found to be 2.8–3 times higher compared to pure iron. It should be noted that the alloy in the study demonstrated limited hemocompatibility (hemolysis ~7%) due to its high Mn content. Severe Plastic Deformation (SPD) treatments have shown promising effects on enhancing mechanical properties and reducing corrosion rates. However, SPD techniques do have certain limitations. Specifically, they encounter challenges when it comes to fabricating certain shapes like thin-walled tubes or ultrafine wires, which are crucial for stent applications.

Additive manufacturing is an emerging fabrication method that holds potential for the processing of biodegradable Fe, making it possible to achieve various surface finishing and complex geometric designs. An in-depth review of the advancements in manufacturing and processing can be found in this recent article [56]. One of the additively manufacturing techniques, to obtain Fe surface with desired defects and grain refinement for degradation, is called cold gas dynamic spraying [58]. It is a high-pressure powder processing technique, utilizing compressed gas to propel metal powder at a large temperature range. The powder impacts the substrate at a high velocity, the particles deform, adhere to the substrate and form a coating. The microstructure can reach grain sizes in the micron to submicron range, resulting in improvement of corrosion rate. It has been shown in the same study that further increase in corrosion rate were obtained after increasing annealing temperature (cf. Table 1, sample treated at 1100 °C, 1200 °C and 1300 °C), based on results of electrochemical tests. Post-annealing, there was an observed increase in the ultimate tensile stress, which elevated to approximately 274–279 MPa. The tensile yield stress fell within the range of 104–139 MPa. These values are similar to those of pure Fe in its annealed state, suggesting a similar load-bearing performance. It was suggested that the acceleration may be attributed to microgalvanic corrosion, due to increased precipitate concentration induced by annealing. The intermetallic phase has been observed and they could act as a cathode in an anodic Fe-based matrix. It is worth noting that the corrosion rate for as-sprayed Fe was higher than annealed ones (Table 1, immersion test results), which should be related to increased porosity and poor interparticle bonding. This resulted in severe corrosion around particle boundaries, probably reducing radial strength and stiffness of stent and leading to premature failure of vessel remodeling.

3.2. Alloying and ion implantation to accelerate Fe corrosion

Alloying is the most common method to tailor metal physicochemical properties. It can be a solid solution of metal elements, in which components are compatible and form a unique phase (single crystal structure), as defined by IUPAC (International Union of Pure and Applied Chemistry). It could also be a mixture of metallic phases, namely, two or more solutions forming a microstructure of different crystals within the metal. For Fe-X alloys, by alloying with X = Cr, Ni, Mo, Cu, Ti, V, and Si, the corrosion resistance of inox can be improved [36]. Various techniques have been reported for Fe-X alloys manufacturing. Research laboratories typically employ methods such as vacuum induction melting, arc-melting, and powder sintering to fabricate small quantities of alloys for property testing [56]. Desired alloy compositions are achieved by repeated remelting of a carefully weighted mixture of pure elements or through the use of master alloys. To improve the quality of the final alloys, a combination of different melting techniques can be applied. Emerging additive manufacturing techniques, such as laser or electron beam methods, can also be employed to create alloys (not using pre-alloyed powders). This is achieved by using a mixture of pure element powders to attain the desired composition or a gradient thereof. However, techniques that utilize powders can often contain higher amounts of impurities, such as oxygen, carbon, or nitrogen. This is due to the large specific surface of the powder, and the inherent challenge of preventing contamination. Despite these points, powder-based techniques permit structural porosity and geometric complexity, aspects that conventional melting and casting methods can struggle with. The choice of the appropriate fabrication technique is closely tied to the research purpose. For studies investigating the relationship between chemical composition and properties, non-powder techniques are preferred to minimize influences from impurities, composition inhomogeneity, and structural defects. Conversely, research with a higher tolerance for impurities can fully leverage the flexibility offered by powder-based techniques for factors beyond mere chemical composition.

As-rolled and as-cast Fe-X (X = Mn, Co, Al, W, Sn, B, C and S) alloys have been studied in *Zheng*'s group [36]. Their results showed that, except Sn, all the other alloying elements could result in the strain hardening effect, i.e. the stress increase from yield to ultimate strength of iron (Fig. 4a and b). Actually, if these two values are very close (for example the pure iron, cf. Fig. 4a and b), the fracture could easily take place during expansion of the stent [59] due to premature necking effect, i.e. the strong strain localization led by lack of strain-hardening. Therefore, the increased difference between yield and ultimate strength in Fe-X alloying favors future application as coronary stents mechanical properties. The elongation values for Fe-X alloys (except Fe–Sn) are higher or comparable to pure iron. It indicates that these alloys can exhibit enough ductility to allow plastic deformation of the stent, which is required to permanently expand the stent to a larger diameter in order to re-open the narrowed artery and importantly to bear the radial force exerted from the expanded artery. These results provide insights on mechanical properties of Fe-based alloys, facilitating the selection of proper materials for stent. The corrosion rate of Fe-X (X = Mn, Co, Al, W, B, C and S) has been investigated by electrochemical, static and dynamic immersion tests. The CR values, derived from electrochemical tests for Fe-X (X = Co, Al, W, B C and S), and those from static immersion tests for Fe-X (X = Co, W, C, S), are increased (but in the same magnitude) with comparison of pure iron. However, the results from dynamic immersion tests show a reduced corrosion rate for Fe-X (X = Mn, Co, Al, W, B, S), and only as-rolled Fe–C exhibits increased CR value. Other researchers reported also increased corrosion on Fe-X binary alloys, such as Fe-Zn [60], Fe–W, Fe-Carbon nanotubes (CNTs) [38] and porous Fe–W layer on Fe skeleton [44]. Therefore, alloying is a promising strategy to accelerate the corrosion Fe, but more efforts should be devoted to increase corrosion rate to a higher magnitude.

The possible approaches to achieve faster corrosion of Fe-X alloy could be: (i) increase of alloying content. For example, Fe alloying with 20–35 wt% of Mn ($Fe_{80}Mn_{20}$ and $Fe_{65}Mn_{33}$ alloy) could be 2-times faster than pure Fe, induced by formation of numerous pits (by galvanic corrosion) on the entire surface [18]. Besides, $Fe_{65}Mn_{35}$ alloy exhibits also improved corrosion rate (5-fold higher, Table 1) compared with Fe [63]. Interestingly, the addition of Ag (1 wt%) in the alloy could boost corrosion rate, achieving 15-times more rapid than Fe. Another example is increasing alloyed Mg and Zn contents [61]. As listed in Table 1, the corrosion potential and current density of $Fe_{60}Mg_{30}Zn_{10}$ alloy is respectively lower and higher than reference Fe, $Fe_{87}Mg_9Zn_4$ and $Fe_{74}Mg_{19}Zn_7$ due to a uniform degradation behavior. As shown in Fig. 4c, more corrosion products and surface cracks can be observed on $Fe_{60}Mg_{30}Zn_{10}$ after immersion tests. (ii) Modification of surface morphology. As reported by *Donic* et al., the corrosion can be significantly accelerated (over 10-folds, Table 1) on a laser-textured Fe–Mn surface with respect to Fe (cf. Fig. 4d) due to increased surface area and formation of Mn-containing oxides on the surface (e.g. Fe_2O_3 and FeO) [47]. It is worth to note that the surface Fe oxides layer has been reported for favoring Fe degradation [42]. *Sun* et al. have also observed increased corrosion rate on pulsed-laser modified Fe–Mn surfaces [64] (Table 1). (iii) Alloying with noble metals, such as Pt, Pd, Au, Ag, to establish micro-galvanic corrosion [48,50]. These materials usually have smaller grain size with respect to pure Fe, showing a large number

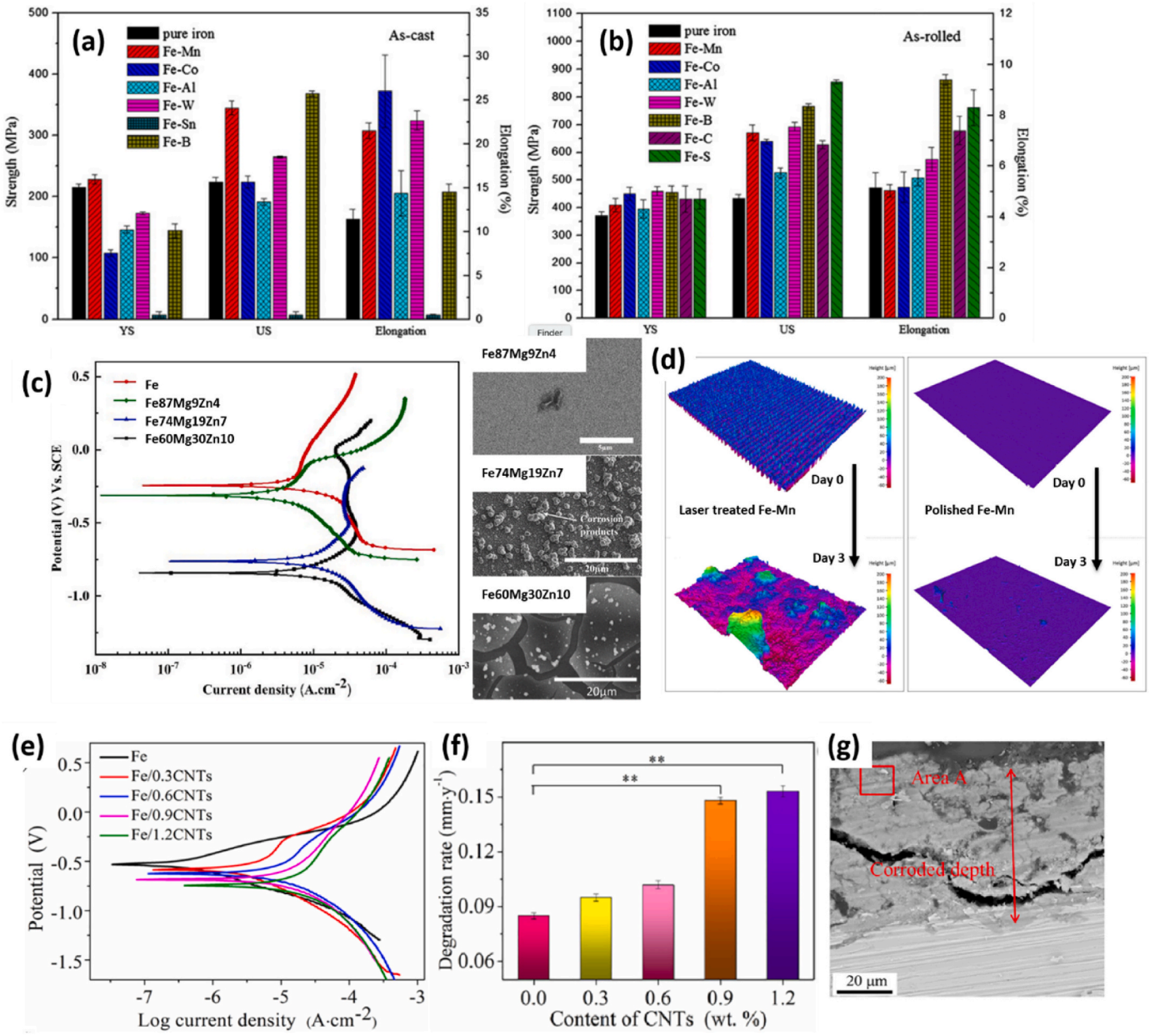

Fig. 4. The yield (YS), ultimate (US) strength and elongation values of (a) as-cast and (b) as-rolled Fe and Fe-X (X = Mn, Co, Al, W, Sn, B, C and S) alloys. Adapted from Ref. [36], copyright 2011, Elsevier. (c) The potentio-dynamic polarization curves and SEM images after static immersion tests of 24 h for Fe, $Fe_{87}Mg_9Zn_4$, $Fe_{74}Mg_{19}Zn_7$ and $Fe_{60}Mg_{30}Zn_{10}$ alloys. Adapted from Ref. [61] copyright 2022, Elsevier. (d) 3D height image representing the surface topography of laser-textured and polished Fe–Mn sample before and after 3 days of immersion. Adapted from Ref. [47] copyright 2018, Elsevier. (e) Polarization curve for Fe and Fe/CNTs alloys (0.3–0.9 wt% CNTs contents). (f) Corrosion rate from 28 days' immersion tests for Fe/CNTs samples and (g) SEM image for Fe/1.2CNTs sample after immersion test. Adapted from Ref. [62], copyright 2019, Elsevier.

of corrosion pits with uniform distribution on the surface after immersion tests. Compared to pure Fe, the corrosion rate enhancement can be achieved 1.4–3.5 folds (Table 1). As shown in Table 1, the ultimate tensile stress was 445 MPa and 503 MPa, respectively for Fe–Pd and Fe–Pt alloys. Compared with Fe (148 MPa), the mechanical strengths are improved. The compressive yield stress of Fe–Pd and Fe–Pt was 745 MPa and 785 MPa, indicating a strength level higher than the currently used high-strength alloy (CoCr L605) in thin-strut coronary stents. For Fe–Ag and Fe–Au alloys (cf. Table 1), the tensile yield stress was in the range of 200–350 MPa, comparable to as-sintered Fe (250 MPa) and higher than as-cast Fe, showing less strengthening effect from Ag or Au additions than expected. (iv) Alloying with an element more susceptible to corrosion, such as Mn, Zn, etc., can reduce the potential of Fe alloys and thus increase corrosion rate. Among these elements, Zn has attracted large interests due to its biocompatibility [60]. In addition, when the content of Zn in Fe is higher than the equilibrium concentration, it might form supersaturated solid solution, increasing Gibbs free energy and thus corrosion sensibility of Fe alloys [60]. As reported in literature [60], the corrosion rate of Fe–Zn alloys (Zn content of 2.1–7.2 wt%) could be 1.3–2.3 higher than reference Fe (Table 1). (v) Multi-component alloys to create intermetallic corrosion. For example, the addition of Pd or Ag in Fe–Mn alloys to generate multiple galvanic reactions between Fe–Mn phase and secondary phase (Pd, Ag) [19,65,66]. As listed in Table 1, the degradation of ternary Fe–10Mn–1Pd can be 3.6-times faster than binary Fe–10Mn, and 15.6-times than reference Fe. Similarly, the corrosion of Fe–30Mn–Ag is accelerated 1.7-fold with comparison of Fe–30Mn and Fe. From Table 1, the ultimate tensile stress and tensile yield stress of Fe–10Mn–1Pd were increased to 1450 MPa

and 650 MPa, higher than Fe–10Mn and reference carbon steel, demonstrating very promising strength properties for designs minimizing alloy volume in load-bearing bioresorbable implants. (vi) Alloying with nanostructured carbon, such as carbon nanotubes (CNTs). According to literature [62], the merits of CNTs can be concluded as their higher standard potential than Fe with excellent conductivity and large surface area, which can generate multiple and efficient Fe galvanic corrosion in nanoscale. In this work, the corrosion potential of Fe/CNTs, derived from polarization curves (Fig. 4e) was negatively shifted by −62 mV, −95 mV, −150 mV and −179 mV with the increase of CNTs content (0.3–0.9 wt%), compared with Fe (Table 1). The corrosion current is also increased after alloying with CNTs (Table 1). After 28 days' immersion test, as shown in Fig. 4f and Table 1, the CR value is gradually increased in function of CNTs content. The SEM image (Fig. 4g) of Fe/1.2CNTs (1.2 wt% of CNTs) sample exhibited thick corrosion layers (confirmed by EDX analysis in area A in Fig. 4g) with corrosion holes and cracks due to localized corrosion.

Ion implantation. Another alternative approach to enhance Fe corrosion rate is surface alloying by ion implantation. Such a technique aims to modify surface physical, chemical, or electrical properties of materials. Briefly, the ions are electrostatically accelerated to a high energy and then impinge onto a target substrate. The average penetration of ions in depth, called ions range, usually varies from 10 nm to 1 μm [67]. This technique, widely used in semiconductor device manufactory, has attracted interests for BRS fabrication. The idea is to modify the Fe surface by metals with lower corrosion potential, generating a galvanic layer on the surface. Recently, Zn and Ta have been reported as ion implantation sources to improve the corrosion rate of Fe [45,49,68]. *Huang* et al. have homogeneously implanted Zn (2.67 wt%; 2.29 at.%) onto Fe (Fig. 5a) with ions range of 60 nm based on SEM-EDX and Auger electron spectroscopy [68]. The highest Zn content of 11 at.% appeared at 30 nm in depth. The ZnO presented on the surface (< 7 nm) whereas Fe–Zn solid solution was claimed beneath. As derived from polarization curves (Fig. 5b), the corrosion potential of Zn-implanted Fe was negatively shifted to −0.901 V, with comparison of pure Fe at −0.582 V (see Table 1). The corrosion current was 3.4-fold higher after Zn implantation. The smaller transfer resistance was measured on Zn-implanted Fe, using EIS, indicating the faster corrosion rate with respect to pure Fe.

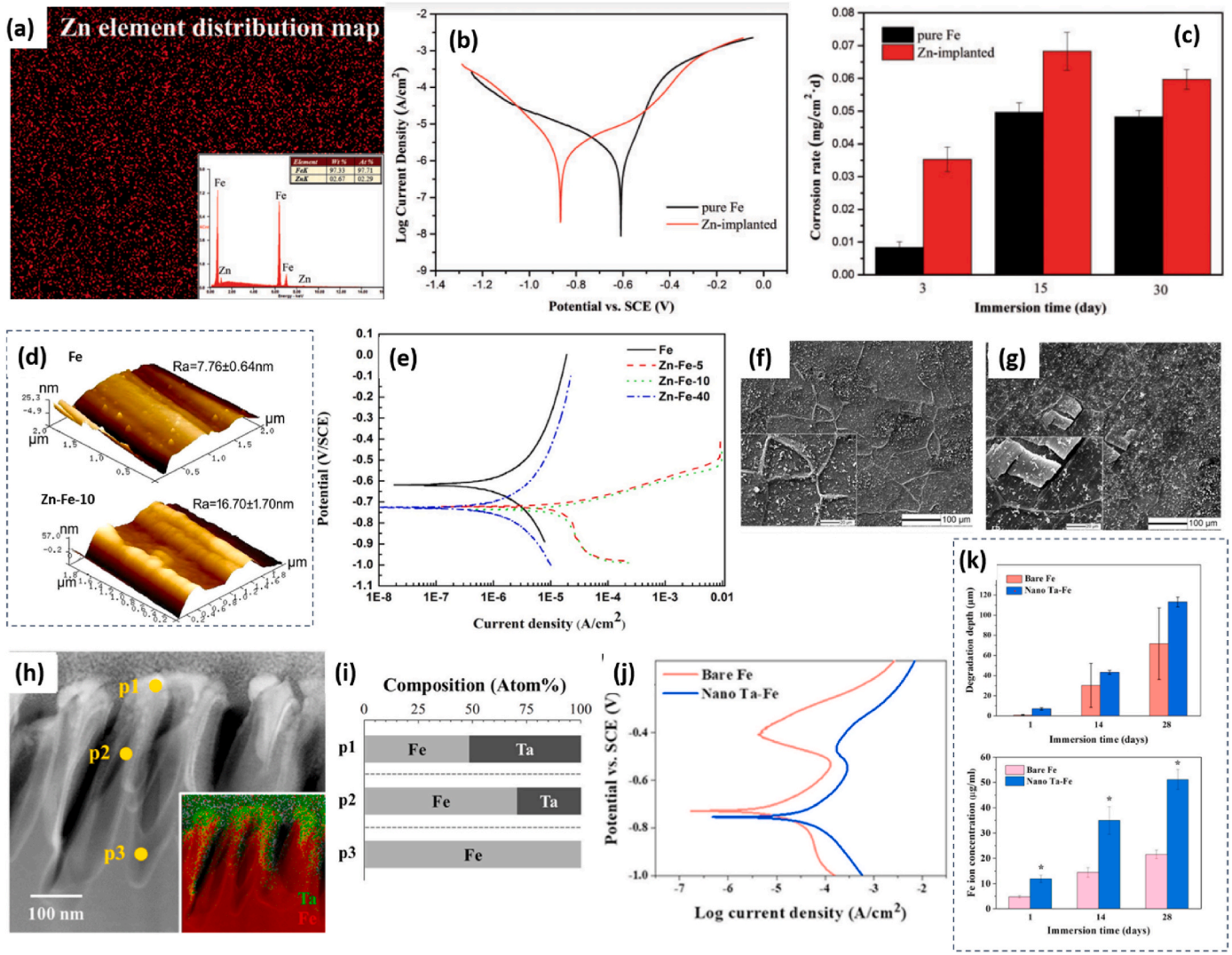

Fig. 5. (A) The EDX mapping of Zn ion implanted Fe; (inset) the mass and atomic contents of Fe and Zn in the mapping area. (b) Polarization curves and (c) static immersion tests for pure and Zn-implanted Fe. Adapted from Ref. [68] copyright (2016), Oxford University Press. (d) AFM image with surface roughness (Ra) values for pure and Zn-implanted Fe (Zn–Fe-10 sample, ion dose = 10×10^{16} ions/cm^2). (b) Polarization curves and SEM images for (f) Fe, (g) Zn–Fe-10 sample after 9 days immersion test. Adapted from Ref. [49] copyright 2017, Elsevier. (h) SEM image and (inset) EDX map for Ta–Fe sample. (i) The atomic composition of Fe and Ta at P1, P2 and P3 points in the SEM image. (j) Polarization curves, (k) analysis of average degradation depth and released Fe ion concentration during static immersion tests for Fe and Ta–Fe sample. Adapted from Ref. [45] copyright 2022, Elsevier.

The static immersion tests showed significantly (over 3 times) higher CR value than pure Fe for the first 3 days, but such a difference reduced gradually at day 15 and day 30 (Fig. 5c). Later, *Wang* et al. reported similar results on Zn-implanted Fe [49]. They found an outmost surface of Fe_2O_3/ZnO oxides after implantation, and the depth of Zn varying in 40–60 nm depending on ion doses. The surface roughness after treatment was increased, as shown in Fig. 5d. The corrosion potential from potentiodynamic polarization curve (Fig. 5e) was negatively shifted from −0.648 V to around −0.7 V after implantation (Table 1), independent to ion doses (sample Zn–Fe-5, Zn–Fe-10, Zn–Fe-40, corresponding to Zn dose = 5×10^{16} ions/cm^2, 10×10^{16} ions/cm^2 and 40×10^{16} ions/cm^2). However, the most intense corrosion current density could be achieved on Zn–Fe-5 (ca. 26.07 μA cm^{-2}) and Zn–Fe-10 (ca. 21.07 μA cm^{-2}) samples, which is 10-fold increased than Fe (ca. 2.19 μA cm^{-2}) and Zn–Fe-40 (ca. 2.01 μA cm^{-2}) (Table 1). After 9 days' static immersion tests, the surface morphology was investigated by SEM. As shown in Fig. 5f, grain boundaries and some white precipitates presented on the pure Fe surface, whereas thick corrosion layers with large cracks were detected on Zn–Fe-10 sample (Fig. 5g). This indicates faster corrosion rate on Zn-implanted samples. Another example is Ta ions implanted Fe [45]. The implantation of Ta ions generates surface nano-galvanic couples and thus accelerate Fe degradation. As shown in SEM and EDX map Fig. 5h, the Ta was mostly dispersed at the top region of nanostructured Fe (nanoridges). The ion contents in 3 points in depth (P1, P2 and P3) was listed in Fig. 5i, confirming ca. 50 at.% of Ta distribution on the outmost surface, ca. 30 at.% at ca. 120 nm in depth and 0 at.% at ca. 300 nm under the surface. As summarized in Table 1, the corrosion potential derived from Fig. 5j shifted toward a more negative direction by −26 mV after implantation, and the corrosion current density was increased from 4.92 μA cm^{-2} for Fe to 13.84 μA cm^{-2} for Ta–Fe. The electrochemical corrosion rate was more than 2-times higher on Ta–Fe with respect to Fe sample. After a static immersion test, as depicted in Fig. 5k, the released Fe ion concentration was 51.0 μg/mL, which was 228% higher than that of bare Fe (22.4 μg/mL) on Day 28. It is worthy to note that the release of Ta ions was not detected during this period. By analysis of the samples after immersion (using SEM), the corrosion depth on Ta–Fe is much higher than on Fe along the entire immersion test (Fig. 5k). One should note that the variation of this value is smaller in Ta–Fe, mainly because of its uniform degradation behavior rather than Fe. The tensile strength (cf. Table 1) could keep constant on Ta–Fe after 12 and 40 weeks of immersion in simulated body fluid, showing more stable mechanism properties than the reference Fe where this value was decreased by about 32%. The value of ultimate tensile stress of Ta–Fe can be kept in the range of 170–177 MPa during 40 weeks, while the value of reference Fe dropped from 180 MPa in week 0–122 MPa in week 40 (Table 1). This fact showed stable mechanical stability of Ta–Fe sample.

3.3. Surface coating of inorganic and organic layer

Coating of inorganic layer. The control of surface topography is an efficient approach to increase Fe corrosion. In this case, the surface of Fe is usually patterned by a galvanic layer. For example, Pt or Au disc arrays have been coated on Fe by lithography [20], as shown in Fig. 6a (Pt arrays) and Fig. 6b (Au arrays). In both works, Fe was coated with different sizes of noble metal layers to study the impact of the layer morphology. The Pt circles discs with Φ20 μm × S5 μm (Φ20 μm = diameter of the platinum discs, S5 μm = the space between two nearest platinum discs) and Φ4 μm × S4 μm were prepared [21]. The quasi-circular template with 200 mesh (200 × 200 μm^2) and 400 mesh (50 × 50 μm^2) were used for Au arrays deposition [20]. From the results derived from polarization curves (Fig. 6c and **d**), the corrosion potential of both Pt- and Au-coated Fe was negatively shifted, and corrosion current was increased, with respect to the reference Fe sample (see data summarized in Table 1). These facts indicated that the corrosion rate was enhanced. According to static immersion tests, the CR value for Pt-coated Fe was improved ca. 2–3 folds (Fig. 6e, Table 1) within 28 days, one can also observe the disc size affecting corrosion speed: the

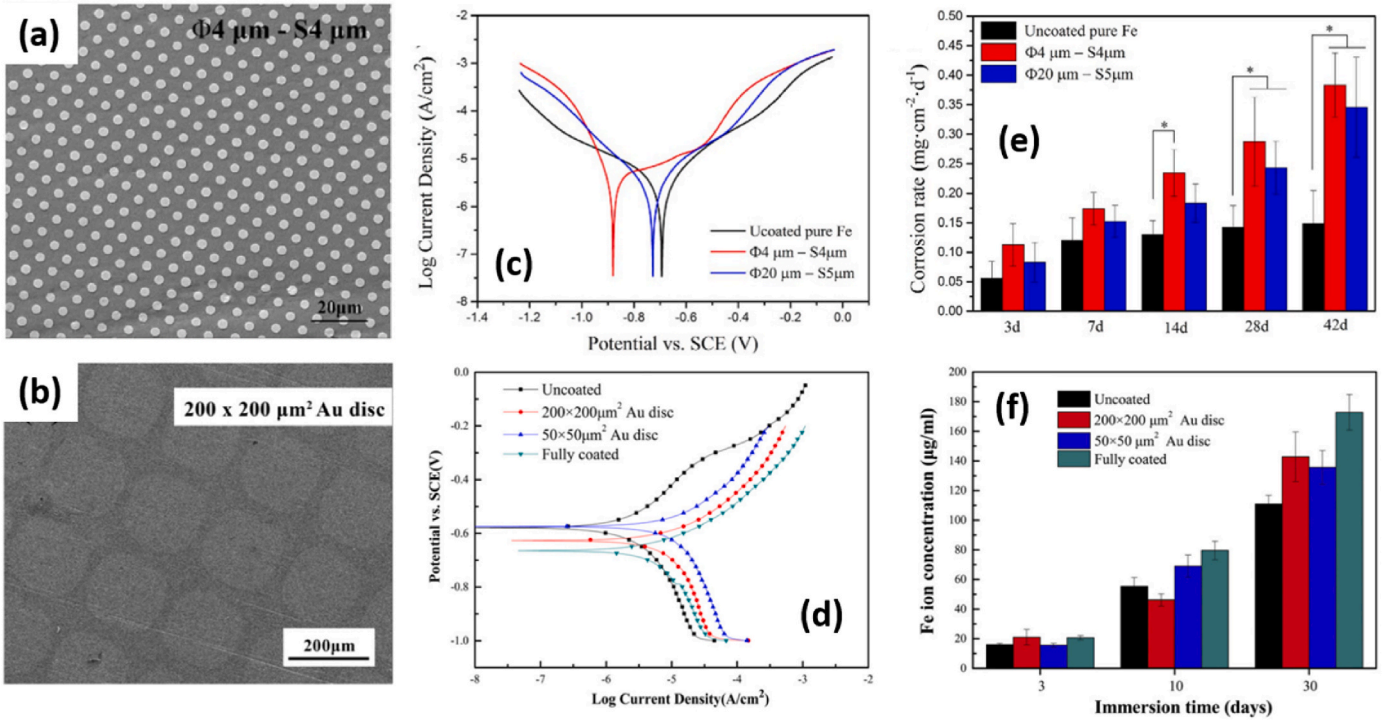

Fig. 6. SEM images of (a) Pt- (discs diameter of 4 μm; the space of 4 μm between two nearest platinum discs) and (b) Au-coated (prepared by a quasi-circular template with 200 × 200 μm^2 size) Fe. Dynamic-potentio polarization curves for (c) Pt- and (d) Au-coated Fe. (e) The corrosion rate values from static immersion tests for 42 days for Pt-coated Fe. (f) Released Fe ion concentration during 30 days immersion test for Au-coated Fe. (a, c, e) Adapted from Ref. [21] copyright 2016, Springer Nature. (b, d, f) Adapted from Ref. [20] copyright 2015, Elsevier.

smaller Pt size (Φ4μm × S4μm) the faster corrosion rate. The Au-coated Fe released ca. 1.3–1.7 times more Fe ions than bare Fe (Fig. 6f). It seems that the Au disc size has negligible effect on the CR values, since more released Fe ions were detected on 50 × 50 μm^2 sample than 200 × 200 μm^2 one at day 10, but the tendency was inverse at day 30. The Au fully coated Fe showed the fastest degradation at day 10 and day 30 in immersion tests. The corrosion behavior of Au-coated Fe is summarized in Table 1. It is worth noting that both Pt and Au coating was observed gradually peeling off during immersion test, and no more Pt or Au can be detected at the end of immersion test. This could be explained as gradually expansion of Fe corrosion beneath galvanic layer, finally leading to the falling-off of coating.

Coating of organic layer. In 2015, poly (lactic-*co*-glycolic acid) (PLGA) infiltrated and coated porous iron was reported for increased corrosion rate over bare porous samples (Table 1), which might be applied as temporary medical implants [69]. The mechanical properties (see ultimate tensile and yield stress in Table 1) of PLGA treated porous Fe was only slightly increased, compared with no-treated porous Fe. This demonstrates that the surface modification had limited impact on mechanical properties of Fe matrix. Later in 2018, surface deposition of polylactide (PLA) was also published for acceleration of Fe corrosion [22]. The mechanism could be attributed to (i) local pH decreasing and (ii) inhibition of passivation layer formation [51,69] induced by PLA surface layer. Compared with bare Fe and poly (methyl methacrylate) (PMMA) coated surfaces, the local pH of PLA-coated Fe was decreased (Fig. 7a), which should be related to degradation (hydrolysis) of PLA

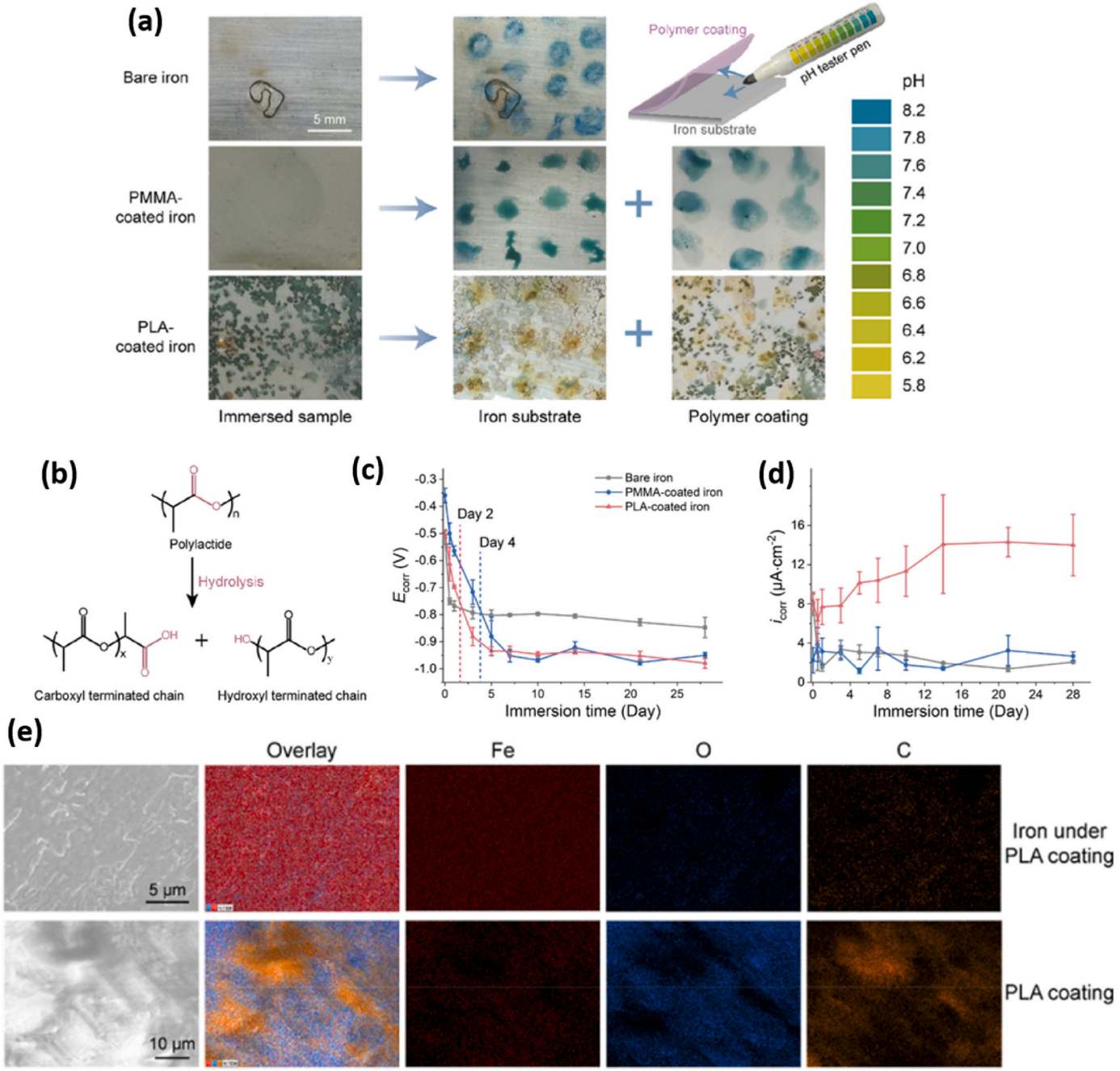

Fig. 7. (A) Local pH on the surface of bare iron, in the interfaces of PMMA- and PLA-coated iron after 24 h immersion in Hank's solution. (b) Illustration of hydrolysis of PLA. Corrosion (c) potential and (d) current, derived from polarization curves, for bare, PMMA- and PLA-coated Fe after immersion in Hank's solution. (e) SEM and EDX mapping for PLA-coated iron after immersion (72 h in Hank's solution). Adapted from Ref. [51], copyright 2019, American Chemical Society.

(Fig. 7b). From day-by-day polarization results (Fig. 7c), the corrosion potential and current of PLA-coated Fe were respectively higher and lower than bare one at day 0 (see E_{corr} and J_{corr} values in Table 1). After 5 day's immersion in Hank's solution, the PLA-coated sample showed lower corrosion potential with respect to the uncoated one, indicating PLA-functionalized sample should be easier corroded. Besides, the corrosion current became higher, demonstrating higher CR value than bare Fe (Fig. 7d). Compared with nondegradable PMMA-coated sample, the Fe corrosion was obviously faster on PLA-coated Fe since day 0 (namely, lower E_{corr} and higher J_{corr} values for PLA-coated Fe, Table 1). After immersion tests, no Ca and P elements were detected on the surface of iron and the interior surface of the PLA coating (Fig. 7e). In addition, no peeling of PLA was reported after immersion test of 28 days, indicating robust coating on Fe surface.

3.4. Overview of mechanical properties of Fe-based materials with accelerated corrosion

As listed in Table 1, mechanical properties of bulk Fe alloys and structure/surface engineered pure Fe, e.g. porous Fe, fine-grain Fe, ion-implanted Fe and coated Fe, exhibit considerable differences under tensile tests as well as compressive tests. The tensile yield stress of pure Fe is about 150 MPa at room temperature, but the alloyed Fe can reach up to 850 MPa under the same test condition. The fact demonstrates that the Fe-based materials are highly tunable on the mechanical strength because Fe system can benefit from various strengthening effects such as solution strengthening, precipitation strengthening, thermomechanical strengthening and microstructural engineering. The large range of mechanical strength provides possibilities for Fe-based materials to answer to different mechanical requirements for different implant applications. For load bearing implants such as cardiovascular stent, high tensile strength and excellent fatigue resistance are required to withstand the radial pressure from the artery. The high strength Fe can reduce the size of the implant to provide enough force, which in turn reduces the requirement of dissolution rate because of the reduction of the Fe volume to be dissolved. Therefore, the strength of different Fe materials via different processing technologies summarized in Table 1 may affect correspondingly the geometrical design of the implant, thus influencing the optimal dissolution rate for the total absorption of the implant in a given duration.

4. Biosafety of Fe-based stent

The development of new metallic resorbable stents requires an exhaustive study of their biocompatibility throughout the entire degradation process. To consider their clinical application, Fe-based devices should not generate toxic degradation products (neither soluble nor insoluble), should not interfere with blood homeostasis and should not cause chronic inflammatory responses.

Since Fe is present in tissues and blood under physiological conditions (45–55 mg Fe/kg bw), it was postulated that corrosion by-products of Fe stents will not cause systemic toxicity and that will instead be metabolized and safely excreted by natural mechanisms. In the physiological environment under aerobic conditions, the redox reaction of Fe^{2+} to Fe^{3+} exhibits a favorable redox potential (+772 mV) [70].

This oxidation enables many fundamental biochemical cellular reactions and transforms iron into an essential element. The produced extracellular Fe^{3+} is practically insoluble and is carried by the specific iron chelators, as transferrin (Tf) towards the cell membrane. Then, through the cellular uptake mediated by the TfR1 receptor, it is transported into the endosomes. However, the total iron-binding capacity of plasma transfer proteins is limited and the presence of excess iron poses a threat to cells and tissues; its toxicity is largely based on its ability to catalyze the generation of radicals. Moreover, the redox reactions of iron constitute a potential danger since they are at the origin of the production of reactive oxygen species (ROS) which, in high concentrations, lead to a cellular oxidative stress. Therefore, the concentration of iron must be tightly controlled and the degradation process from the Fe based-stents should not release excessive amounts of iron in a short period.

4.1. Biocompatibility studies

1) Cellular studies in contact with iron under *in vitro* static and dynamic conditions

In vitro studies are not representative of *in vivo* conditions of tissues in contact with stent material; however, when suitable models are used, they provide a first step to assess biocompatibility.

Methodological approaches based on the addition of Fe^{3+} solutions into the cell culture media were used to simulate the Fe corrosion products and to study their effects on the cell viability. By this method it was shown a significant decrease in the mitochondrial activity (> 2 mM of Fe^{3+}) and lipid peroxidation correlated to the Fe^{3+}concentration on CHO–K1 cells [71]. The absence of toxicity of iron solutions incubated 1–3 days on endothelial cells was reported for the concentrations < 50 mg/mL [72].

However, the Fe degradation compounds released from medical devices are generally studied following ISO 10993-5 by direct or indirect contact tests [73]. The ISO 10993-5 standard references the conditions for obtaining the released products (cm^2 or mg of samples/mL extractant), the cytotoxicity tests and the choice of cell lines [73]. Preconized cell lines are often from rodents, such as BALB/3T3 (CCL-163™) fibroblasts, J774A.1 macrophages (TIB-67™) or CHO–K1 (CCL-61™) epithelial cell line, that are not representative for the study of stent surrounding tissues but recommended for toxicology evaluations. Few studies have assessed human models relevant to vascular stent applications, such as human endothelial cells HUV-EC-C (CRL-1730), or primary cells as smooth muscle cells (SMC) and adipose tissue-derived stem cells (ADSCs).

Assessments of the cytotoxicity of compounds released during Fe corrosion are often performed by placing Fe samples in physiological buffer or culture medium and, at the endpoints, the released products are added to the cells (Fig. 8a). Another methodological approach evaluates compounds released from Fe samples placed in culture inserts. These supports have a permeable polymeric membrane (polyethylene terephthalate, polyvinylidene difluoride or nitrocellulose among others) with pores of variable size allowing the diffusion of soluble compounds (Fig. 8a). The cell viability is measured after incubation times (in general comprise between 24 and 72 h) by the evaluation of the metabolic enzymatic activity using test as MTT ((3-(4,5-dimethylthiazol-2-yl)-2,5-diphenyltetrazolium bromide), Alamar blue etc. (Fig. 8) [36,72,74]. Others parameters as morphology, reactive oxygen species (ROS) production [29], gene expression [75] and cell proliferation are also evaluated. There is a consensus regarding the absence of toxicity of the soluble iron degradation products on several types of cells as fibroblasts [48,75–77], CHO–K1 [71], human endothelial cells [38,72], smooth muscle cells [35,36] and ADSCs (Fig. 8b) [74]. These studies showed that the cellular metabolic activity was not affected by the presence of soluble degradation products after 24–72 h. However, a reduction in cell proliferation was reported on smooth muscle cells, which was considered as a positive point, since these cells are the main responsible for in-stent restenosis [35,78].

Direct contact tests between iron surfaces and cells evaluate the impact of solid residues produced during corrosion on the fate of cells and tissues. A toxic effect of solid particles produced during iron corrosion was reported on L929 [79], CHO–K1 [71] and BALBc 3T3 fibroblasts [76]. It was recently shown that direct contact of endothelial cells (HUVECs, and Human Aortic) and SMCs (Human Coronary Artery and Human Aortic) with the Fe° as microparticles (50–800 mg/mL) alters cell viability after 24 h of culture for the high range of concentrations. However, contact with soluble release products from the same

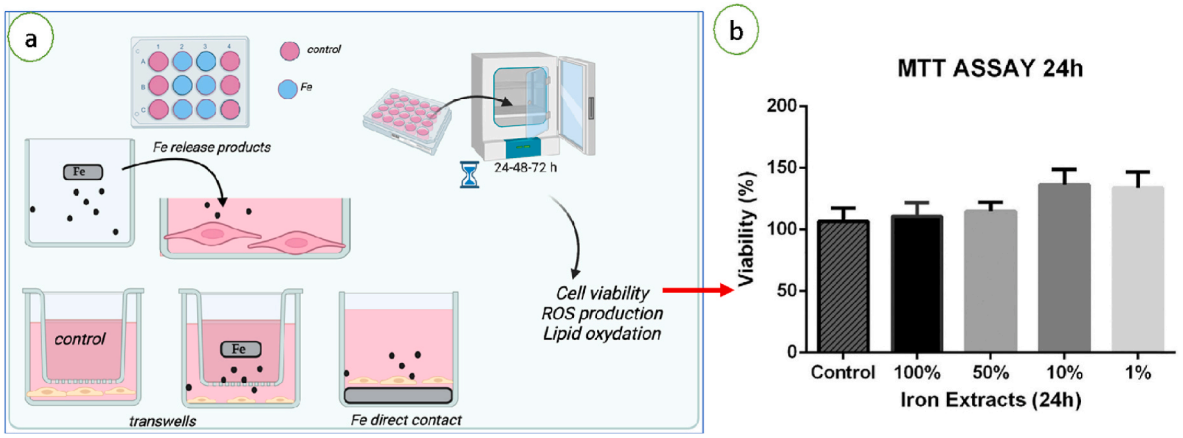

Fig. 8. Schematic representation of *in vitro* tests for the biocompatibility evaluation of Fe samples (a) MTT test of ADSCs for indirect contact evaluation of iron released products (b). Adapted from Ref. [74] for (b), copyright 2021, Elsevier.

samples did not lead to changes in cell viability [29].

Almost all of the *in vitro* evaluations are carried out in culture dishes under static conditions, in these conditions the released Fe ions and ROS can accumulate to a very high concentration. Thus, the local concentration of Fe ions and ROS on the surface of iron samples may be even higher than it will be *in vivo* when the stents are subjected to blood flow. To better mimic *in vivo* conditions, a dynamic environment such as a bioreactor with a dynamic medium circulation system might be more effective in assessing cytotoxicity and corrosion parameters. Thereby, *ex vivo* studies (Fig. 9) under simulated blood flow conditions are developed to consider the influence of shear stress and flow conditions on stents surfaces or to assess the material degradation in dynamic conditions [80]. These systems use mock vessels (Fig. 9a) or whole arteries (Fig. 9b) in order to take into account the complexity of the tridimensional structure of tissues. Dynamic perfusion systems consist in a flask containing the perfusion medium connected to a peristaltic pump to control the flow rate and temperature. The arteries (whole or cut into rings) are placed in culture dishes connected to the system and their viability and morphology are assessed in contact of iron samples at different endpoints. By this method it has been shown modifications on iron surfaces due to physiological flow leading to a higher degradation rate under dynamic conditions [35] (Fig. 9c and d).

2) Influence of physiological parameters on the Fe corrosion

Some parameters of the Fe corrosion evaluation in physiological media, merit to be analyzed. The pH and the ionic concentrations of the simulating physiological fluids are calculated to be closed as possible to those of blood plasma. However, these media often do not contain proteins which are critical components of plasma. It was shown that the use of culture medium containing 10% fetal bovine serum as an extraction vehicle reduced the formation of corrosion products from a nitrided iron stent [79]. Proteins can react with both soluble and insoluble components released during Fe corrosion, but also proteins interact with the surface of the stent and create a layer of adsorbed proteins, as is the case with all devices after implantation [81,82]. The adsorption of proteins to the surface leads to changes in the rate of corrosion and influences the composition of the microenvironment close to the implant conditioning the response of the surrounding tissues. The adsorbed protein layer forms a barrier between the metal surface and the environment leading to inhibition of iron degradation. It was reported that after 7 days of immersion in culture medium without serum, iron samples showed zones completely corroded on the surface and solid deposits in zones close to the sample. The addition of fetal calf serum significantly decreased this corrosion rate [71,76]. The preconditioning of samples in culture medium (2 h–28 days) before contact with cells was carried out to simulate the different stages of iron degradation in the presence of serum proteins and showed a correlation between the preconditioning time and the increase in the thickness of the iron layer

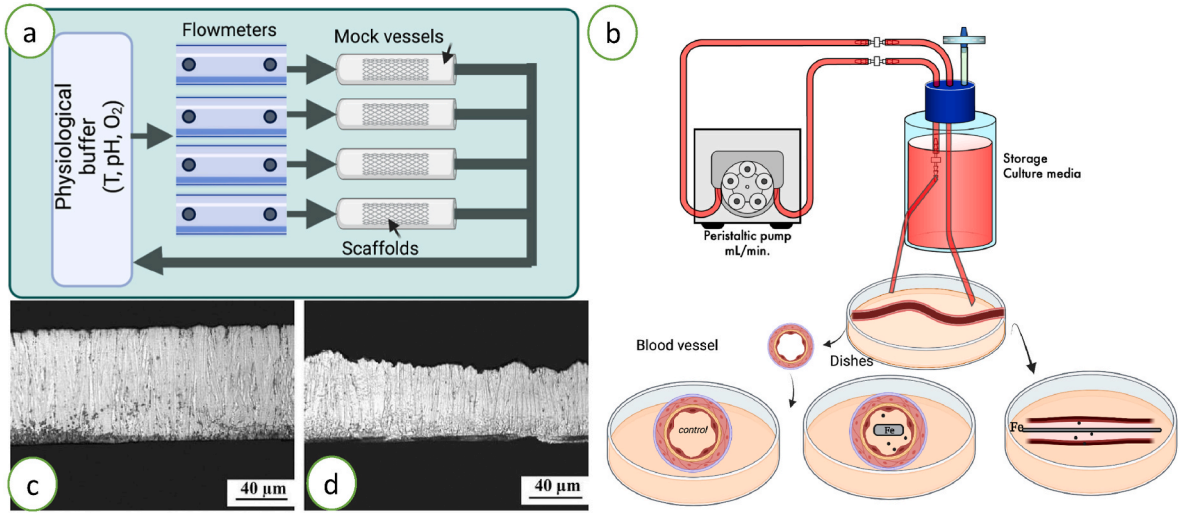

Fig. 9. Illustration of dynamic systems for the evaluation of iron samples. Mock vessels (a) or arteries (b) under simulated physiological flow. Adapted from Ref. [80]. Degradation under static (c) or dynamic (d) conditions of iron surfaces. Adapted from Ref. [35], 2010, Elsevier.

degradation [83]. The authors showed that this degradation layer, whose composition was complex, led to a decrease in the release of ions and showed a positive effect on cell survival at longer culture times, 7 or 28 days [83]. Furthermore, the O_2 and CO_2 concentrations in the culture system were shown to influence the rate of iron corrosion. Some researchers [17] pointed out a direct correlation between the iron corrosion rate and the local O_2 concentration. Regarding the CO_2 content, the tests carried out in culture incubators showed lower % than in the tissues, and therefore does not reflect the *in vivo* conditions. It has been shown that the high CO_2 content leads to an important diminution in the rate of Fe degradation [84].

3) Reactive oxygen species produced during Fe corrosion in physiological environment induce cellular changes

Oxidative stress on surrounding tissues is another aspect that must be considered on Fe devices. During iron degradation under aerobic conditions and neutral pH, Fe^{2+} and H_2O_2 generated participate to the production of HO• radicals, one of most damaging reactive oxygen species (ROS). ROS refers to the extremely reactive molecules and free radicals derived from molecular oxygen produced during aerobic respiration and cellular metabolism as normal byproduct [85]. Moderate amounts of ROS have beneficial effects on several physiological processes like the reduction of malignant pathogens, wound healing, and tissue repair processes by acting as signaling molecules [86,87]. In contrast, ROS overproduction disrupts the body homeostasis inducing oxidative tissue damage.

An overload of iron ions due to excessively rapid corrosion will produce a large amount of ROS by the Fenton reaction, and will induce a cascade of oxidation of cell membrane lipids leading to cellular oxidative stress and Ferroptosis [88]. Under *in vitro* physiological conditions the presence of HO• due to the corrosion of Fe was demonstrated [23]. A deleterious role of HO• on human endothelial cells and SMCs cultured in direct contact with iron powders was confirmed by the authors; they showed that the catalase addition protected cells from the oxidative stress generated by the iron corrosion [29]. An *ex vivo* model of arterial rings directly exposed to an iron rod in the lumen of the artery was developed by the same group to mimic endothelium-stent contact. With this experimental design, they showed a deleterious impact on the endothelium of arteries caused by the presence of HO• ions released during Fe corrosion, followed by a decrease in the enzymatic activity of eNOS and then an inhibition of the production of NO [29]. The protective role of serum in the environment close to stents was highlighted in an *in vitro* study using fetal bovine serum added to the HUVECs exposed to iron powder. The authors also evidenced *in vitro* the blocking of produced ROS during the Fe corrosion by the serum components [89]. To assess the behavior of cells that are *in vivo* involved in the resorption of degradation debris, macrophages were cultured in contact with rings of pure Fe [90]. As the metal degraded, a deposit of insoluble degradation products accumulated near the Fe° ring and in the same area the macrophages showed alterations in morphology and decreased viability, motility and mobility [90].

Different structural and chemical modifications carried out on the Fe to control the biodegradation induced modifications of their biocompatibility, in particular concerning direct contact evaluations. For example, porous iron scaffolds manufactured by direct metal printing showed significant cytotoxicity by direct contact between cells and scaffolds under static culture conditions compared to Ti–6Al–4V, on the other hand, their release products did not induced toxicity (up to 72 h, Figs. 10–1) [40]. Recent work has shown that extrusion 3D printing can provide porous iron scaffolds with random microporous interconnectivity providing many complex sites favorable to autocatalytic corrosion allowing for improved biodegradability. However, *in vitro* studies have shown a decrease in adhesion and cell viability upon

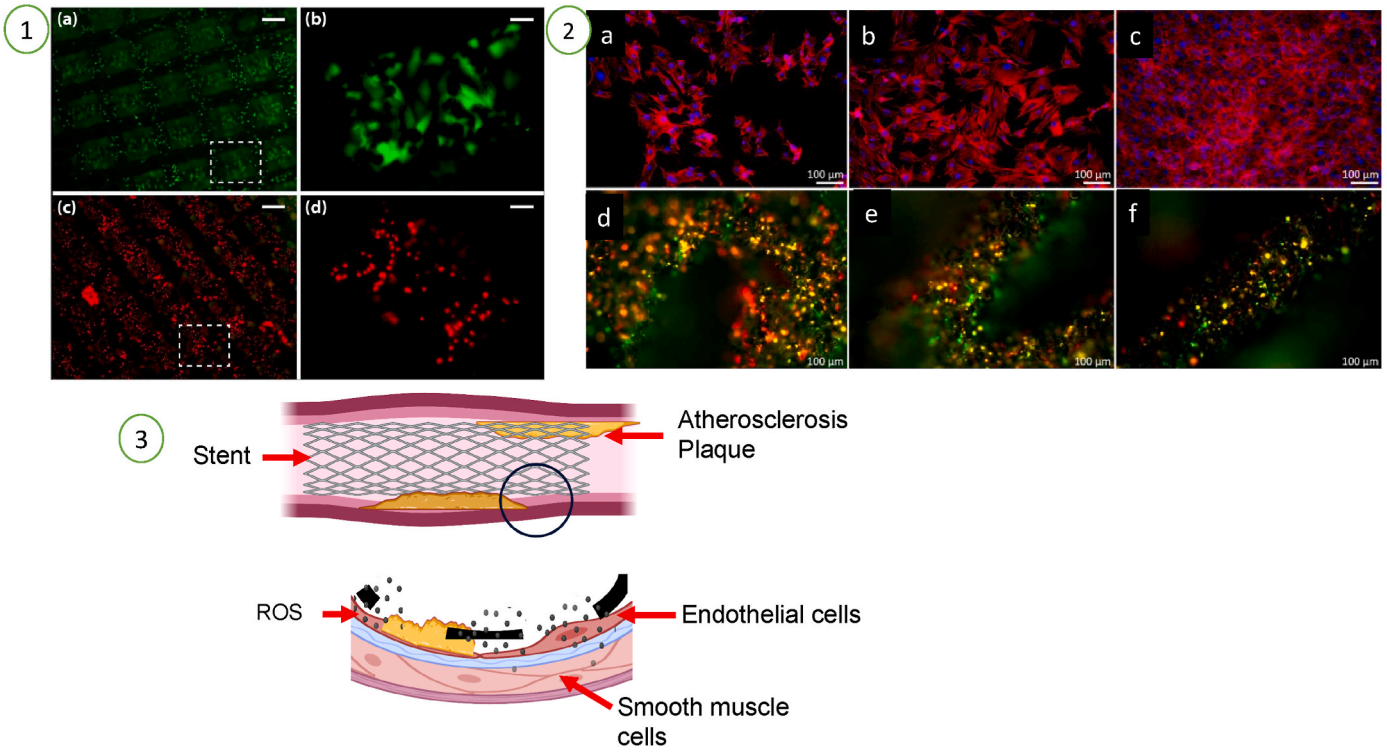

Fig. 10. (1) MG-63 cells on Ti–6Al–4V (a, b) and iron (c, d) scaffolds; live cells, green; dead cells, red. Scale bars indicate 300 mm (a, c) and 30 mm (b, d) (adapted from Ref. [40]). (2) Preosteoblasts after 3 days of culture in (a) 100%, (b) 75%, and (c) 50% iron extracts, (a–c) rhodamine phalloidin (red) and DAPI (blue) stained; morphology of the cells after 3 days of direct cell culture on the iron scaffolds (*d*-f) calcein acetoxymethyl (green, indicating living cells) and ethidium homodimer-1 (red, indicating dead cells) (adapted from Ref. [46]). (3) Corrosion of iron stent produces ROS by the Fenton reaction that can induce a cascade of oxidations on cell components.

contact with scaffolds [46]. Pure iron prepared either by microwave sintering (MSed) with a porous structure or by laser fusion (LMedFe) with a compact structure, both showed higher biodegradation rates (about 44 and 13 times) than those molten Fe. According to literature [91], the corrosion rate based on electrochemical tests of MSed Fe (0.35 ± 0.002 mm $year^{-1}$) is higher than LMed Fe (0.10 ± 0.002 mm $year^{-1}$). The immersion test in Hank's solution for 30 days showed the same trend, namely, more Fe ions releasing from MSed Fe (5.15 μg mL^{-1} day^{-1}) than that from LMed Fe (4.33 μg mL^{-1} day^{-1}). Biocompatibility studies of MSed Fe and LMed Fe did not show any toxic effect (nearly 90% control), nevertheless the studies were carried out only by evaluation of released compounds or indirect contact [91]. In another type of strategy, *Zhang* et al. proposed to use a polymeric coating in Polylactide which accelerates the biodegradation of iron-based stents and showed good biocompatibility *in vitro* and *in vivo* models [89].

Overall, *in vitro* tests show that the soluble released products, in the presence or absence of proteins in the solution, do not appear to be toxic. However, direct contact of cultured cells on iron surfaces could leads to toxicity partly due to solid debris and ROS produced during corrosion process. Interactions at the interface during iron corrosion in biological media deserve to be studied in depth, indeed some observations appear contradictory. On one hand, it was shown that the protein layer adsorbed on the Fe surface reduces the corrosion rate and therefore the rate of ROS production. On the other hand, it was shown the increase of ROS production by a local effect of oxidative microenvironment around the surface and that this ROS excess could be at the origin of an increased local toxicity. To solve this problem, some strategies are being developed on iron and other metallic surfaces using grafts or coatings that use polymers, antioxidants [92], but also nanoparticles such as exosomes [93] to protect the cells and tissues that surround the implant.

4.2. *In vivo studies*

Iron is essential to the human body and makes up 0.04 % of the weight of humans [70]. It is the necessary component of hemoglobin in blood. An adult intake about 1–2 mg of iron through the intestine every day. Transport absorption and storage of iron are well known and alongside with iron mechanical properties, make iron-based alloys favorable candidates to be used as biodegradable implant material. Nevertheless, to demonstrate safety and biocompatibility of Fe-based stents, alongside with *ex vivo* studies, *in vivo* studies are mandatory to take into account shear stress, pH, temperature and continuous pulsatile blood flow. Though some authors try to reproduce *ex vivo* or *in vivo* conditions, those attempts do not reflect biological, chemical and hemodynamical complexity of animal and human bodies. To evaluated iron-based scaffold biocompatibility, before human implantation, it is

Table 2
In vivo studies about Fe-based stents and scaffold.

Ref.	Materials	Strut thickness	Eluting	Animal type	n	Vessel implantation site	Follow-up duration	Monitoring	Results
[94]	Pure Fe	100–120 μm	–	New Zealand white rabbits	16	Descending aorta	6, 12, 18 months	Angiography	No thromboembolic complications, neointimal proliferation, pronounced inflammatory response, and systemic toxicity
[104]	Pure Fe	120 μm	–	Minipigs	27	Descending aorta	1–360 days	Histomorphometry and quantitative angiography analysis	No signs of iron overload or iron-related organ toxicity and evidence for local toxicity
[105]	Pure Fe	–	–	Juvenile domestic pigs	8	Proximal left anterior descending, left circumflex artery, or right coronary artery	28 days	Histochemistry, vessel morphometry	Safe, without inflammation. Brownish tinge. No excessive endothelization
[99]	Pure Fe and nitrided Fe	120 μm	–	Minipigs	18	Left and right iliac arteries	1, 3, 6 and 12 months	Histological examination	No thrombosis, decreased inflammation
[95]	Nitrided Fe	70 μm	–	Minipigs	8 Fe; 8 CoCr	Coronary artery	28 days	Coronary angiography, endothelialization and histological observation	No signs of organ toxicity
[17]	Fe-0.07 N	90 μm	–	New Zealand white rabbits	78	Abdominal aorta	7 days; 1, 4, 6, 9, 12, 24 and 36 months	Endothelialization and histopathologic observation	No adverse events, homogeneous endothelial coverage, slight inflammatory response
[101]	Pure Fe – polymer (MPS)	50 μm	Sirolimus	Small Guizhou pigs	15	Left anterior descending coronary artery and right coronary artery	6, 12 months	Micro-CT, angiography and Optical coherence tomography	No inflammation and good degradation profile of MPS
[89]	PLA coated Fe (MPS)	53 μm	Sirolimus	Minipigs	74 MP S; 68 CoCr	Left anterior descending coronary artery and right coronary artery	1, 3, 6, 12, 24 months	Micro-CT, optical coherence tomography, endothelialization and histopathologic observation	No significant impact on endothelial cells and smooth muscle cells on MPS. No thrombosis observed
[100]	Nitrided iron stents	70 μm	–	Rabbits	6	Right femoral artery	1 and 6 months	Radiographs; cell proliferation and viability	Decreased the neointimal hyperplasia by inhibiting VSMC proliferation induced by corroded granules
[103]	Pure Fe	54 μm	–	Diabetic new Zealand white rabbits	7 Fe 7 stainless S316L	Right femoral artery	6 months	Radiographs; endothelial cell proliferation and viability	Increased in iron-stent degradation and inflammation; decreased re-endothelialization.

then mandatory to explore local biocompatibility looking for inflammation, corrosion rate, oxidation and endothelium healing in animal models and systemic toxicity such as iron-overload within liver, lymph nodes and heart.

Peuster et al. in 2001 [94] were the first researchers to propose iron-based bioresorbable stent for cardiovascular applications. This work used a New Zealand rabbit model for pure Fe scaffold implantation within the descending aorta with a follow-up duration up to 18 months. In vivo monitoring was performed by angiography. It reported a good safety profile with no thrombosis, and no immediate or delayed recoling. After animals were sacrificed, histological exploration showed no excessive intimal proliferation and inflammation with low rate of macrophage. It described brownish deposits of the vascular wall adjacent to the stent. From 2001 to nowadays, 10 *in vivo* studies about Iron-based stents using animal models were reported (Table 2). All authors reported unanimously favorable biocompatibility profile with low thrombosis and stenosis rate, no signs of local or systemic toxicity. Only *Feng* et al. in 2013 showed evidence of inflammation at 3–6 months. When compared to CrCo stents, Iron-based stents exhibited good and homogeneous reendothelialization [95] contrary to first and second generation polymer-based resorbable stents which prolongated neointimal healing and were suspected to cause higher rate of thrombosis compared to drug eluting stents [96,97]. All these works found brownish deposits around struts, which are products of iron degradation. Those corrosion products were reported to have neither local nor systemic toxicity though some authors suggested that they might mediated local oxidative stress through hydroxyl liberation [29,98]. *Zhang* et al. [89] recently reported *in vivo* and *in vitro* results about a new biodegradable iron based metal-polymer composite stent (MPS). They extensively investigated biological biocompatibility emphasizing the importance of using serum and especially albumin to mimic blood-related physiological conditions. They suggested that serum could decrease oxidative damage during iron corrosion. Overall, this work confirmed good biocompatibility of iron-based stents. MPS made of an iron backbone, of a zinc layer and of PLA coating with sirolimus designed to accelerate iron corrosion exhibited *in vivo* satisfactory mechanical properties and good patterns of endothelialization with a follow-up of more than 2 years. Surprisingly they also reported first human implantation with good OCT and clinical results. Clinical trial with 45 enrolled patients has been pursued using MPS [99]. In addition, *Qiu* et al. hypothesized that the corroded granules produced by the iron stent would prevent in-stent restenosis by inhibiting proliferation VSMC [100]. They tested this hypothesis on a rabbit carotid model. Iron oxide, which was the main component of corroded granules produced by stent resorption, decreased the neointimal hyperplasia by inhibiting VSMC proliferation. This result indicated that neointimal hyperplasia is responsible for most secondary stent thrombosis.

Regarding corrosion rate of Fe-based scaffold, all studies found that it is insufficient with large portions of the stent remaining intact after 1 year. Many efforts are being performed to accelerate degradation rate by surfacing functionalization, metal alloying or surface treatment with the objective of complete resorption within less than 2 years. Recently *Li* and co-workers [101] reported a study about Fe-stent functionalized with polymer with higher degradation rate than pure Fe-stent. *Lin* et al. in 2021 [102] studied pure Fe alloyed to nitrogen sprayed with asymmetric sirolimus-loaded poly (D,L-lactic acid) stents and found accelerated corrosion process. Corrosion rate has only been recently quantitatively evaluated in following studies, listed in Table 2: (1) *Lin* et al. first described *in vivo* corrosion rate of bioresorbable nitrided iron stent and plane iron stent after implantation in abdominal aorta of New Zealand Rabbits using mass loss over 36 months [17]. Both of the two mass curves showed gradually decreasing slopes indicating gradually slowing corrosion rate. The nitrided iron stent had significantly high mass loss than pure iron scaffold. At 12 months, mass decreased of 45 % for nitrided stent *versus* 24 % for pure iron one and 76 % *versus* 44 % at 36 months. (2) *Zhang* et al. [89], after implantation of metal-polymer composite stent within coronary arteries of mini-pigs, monitored stent degradation using coronary arteriography, micro-CT and OCT with a follow-up of two years. They reported a weight loss of 20 % at one year and which even reached 50 % at two years in microCT and of 23.3 % and 43.8 % at one and two years respectively. They even implanted this stent in a human reporting a 62.0 % loss of weight at 26 months of follow-up using OCT. (3) *Qiu* et al. tested the hyperglycemia relationship to iron-stent corrosion rate [103]. To do so, they used a diabetic rabbit model and found that hyperglycemia induced increase in iron-stent degradation and inflammation and decreased re-endothelialization of the device. As stents are frequently used in diabetic population, this study raises questions about permeability of those devices in these patients. Besides, other ongoing Fe-based stents trials in cardiovascular application, summarized in Table 3, which aims to depict ongoing cardiovascular application trials about iron-based stents as they might provide new and updated information on degradation properties and biosafety issues. Moreover, it shows that iron-based stents are a dynamic research topic with different functionalization strategies to optimized iron-based stents corrosion pattern within patients. The results of those ongoing studies will determine whether iron-based stents are the next generation bioresorbable stents for human practice. Alongside those efforts, work remains to be done to find a Fe-base alloy or Fe functionalization and treatments to obtain higher corrosion rate, while preserving biocompatibility and mechanical properties of Fe-base stent.

5. Conclusion and perspectives

This review presents a number of examples of Fe-based materials as candidates for bioresorbable stent. The mechanism of Fe degradation is first summarized, emphasizing the importance of corrosion products participating metabolism, and the possibility of potential toxicity related to ROS releasing in this process. Then, the physiochemical approaches to study and determine Fe corrosion rate are introduced. The corrosion rate can be estimated both from electrochemical (potentiodynamic polarization derived Tafel plot) or immersion tests (by weight loss or released ions concentration measurements). Based on information collected from interface behavior (such as corrosion current density, resistance, capacitance, etc.), microstructure (like crystal structure, grain boundary, shape, etc.) and surface (e.g. energy, composition or morphology), the strategies to accelerate Fe corrosion can be divided into 2 categories. (i) For pure Fe, one can generate porous/roughed surface, or tailor Fe microstructure with desired defects/grain refinement to increase active surface for Fe oxidation. The CR value can be usually increased around 10 times for porous/roughed surface iron, and up to 5-folds by fined grain treatment, with respect to reference Fe sample. (ii) For alloyed and surface coated Fe, both noble and abundant ions/atoms, on surface or in matrix, undergoing microgalvanic displacement, can be used to accelerate Fe oxidation. The alloyed Fe is able to increase corrosion rate at least 1.5 times (Fe–30Mn–Ag), achieving ca. 24 times on $Fe_{65}Mn_{35}Ag_1$, *versus* pure Fe. The value is 2–5 time higher on ion implanted Fe and Fe with galvanic surface coating. The organic layer (polylactide) which releases H^+ with local pH decreasing during hydrolysis, can achieve 6-folds faster Fe corrosion. The materials modified by both surface and structural strategies can boost corrosion speed, like surface patterned alloys, where the corrosion rate enhancement can be promoted to 14 times (laser-textured Fe–Mn *versus* Fe), compared with initially 2 times on conventional polished Fe–Mn (*versus* Fe). The combination of multiple strategies might be a very promising route to design novel Fe-based materials for resorbable implants. Recently, there has been a significant surge in interest surrounding Fe-based biocomposite, prepared by incorporating a secondary compound into Fe matrix, such as $CaCl_2$, $CaSO_4$, MnO [106–108]. These compounds, serving as source of Cl^- ion releasing ($CaCl_2$) and micro-acidification ($CaSO_4$), or catalyst to promote oxygen reduction reaction (MnO_2), could increase the corrosion rate of Fe. This makes Fe-based biocomposite promising candidate for bioresorbable and implantable medical device.

Table 3
Ongoing Fe-based stents trials in cardiovascular application.

Trial	Stent	Condition	Study type	Scaffold material	Surface modification	Eluting	n	Expected duration	Last update	Primary endpoint
IRONMANN-II	IBS	Stable Coronary artery disease	Prospective, Multicenter, Randomized, Single Blinded Trial	Iron	–	Sirolimus-Eluting	518	24 months	December 2022	Scaffold late lumen loss at 12 month
GENIUS	IBS	Infrapopliteal Arterial Stenosis	Prospective, Non-randomized, Non-comparative study	Iron	–	Sirolimus-Eluting	120	1 year	March 2022	Primary Patency Rate (180 days)
IRONMANN-III	IBS	Stable Coronary artery disease	Prospective, Multicentr, Randomized, Single Blinded Trial	Iron	–	Sirolimus-Elu ting	1096	24 months	March 2022	Target Lesion Failure at 1 year
IRIS	IBS	Pulmonary Artery Stenosis	Prospective, single group	Nitrited Iron	–	Sirolimus-Eluting	82	24 Months	November 2021	Rate of freedom from in-stent restenosis
A First-in Man Study to Evaluate the Feasability and Safety of IBS	IBS	Stable Coronary artery disease	Prospective, Non-randomized, Non-comparative study	Iron	–	Sirolimus-Elu ting	15	1 year	August 2018	Target Lesion Failure at 1 month

Regarding biosafety, Fe (including structural or surface engineered Fe), the *in vitro* results by indirect contact tests show good biocompatibility of released compounds during Fe degradation on cultured cells (e.g. fibroblasts, epithelial, endothelial cell, smooth muscle cells and adipose tissue-derived stem cells). The direct contact of cultured cells on Fe surface, nevertheless, display toxicity related to solid debris and ROS releasing during Fe degradation. Therefore, the control of ROS might be the main concern for clinical application of Fe-based implants. For *in vivo* animal tests (in white rabbits, minipigs and domestic pigs, from 28 days up to 3 years), most published studies reported excellent biocompatibility profile without local or systemic toxicity, yet slight inflammatory response has been observed at 3–6 months in white rabbits on nitrided iron scaffold. According to these researches, Fe corrosion products around struts did not show impact on biocompatibility. In addition, all *in vivo* evaluations showed large portions of stent remained intact after 1 year of implantation, the further acceleration and control of Fe degradation is highly desirable and should be validated in animal tests.

Source of support

Any grants/equipment/drugs, and/or other support that facilitated the conduct of research/writing of the manuscript including AFMRC project details, if applicable):

- Financial support from Agence Nationale de la Recherche, project BIORESORB ANR-21-CE18-0012, coordinator: Yun Luo.
- Scholarship granted to Yang Zhang from China Scholarship Council, grant's number: CSC 202106340022.

Funding

Funding was received for this work: Agence Nationale de la Recherche (BIORESORB, ANR-21-CE18-0012)

Intellectual property

We confirm that we have given due consideration to the protection of intellectual property associated with this work and that there are no impediments to publication, including the timing of publication, with respect to intellectual property. In so doing we confirm that we have followed the regulations of our institutions concerning intellectual property.

Research ethics

We further confirm that any aspect of the work covered in this manuscript that has involved human patients has been conducted with the ethical approval of all relevant bodies and that such approvals are acknowledged within the manuscript.

IRB approval was obtained (required for studies and series of 3 or more cases).

Written consent to publish potentially identifying information, such as details or the case and photographs, was obtained from the patient(s) or their legal guardian(s).

Authorship

All listed authors meet the ICMJE criteria.
We attest that all authors contributed significantly to the creation of this manuscript, each having fulfilled criteria as established by the ICMJE.

We confirm that the manuscript has been read and approved by all named authors.

We confirm that the order of authors listed in the manuscript has been approved by all named authors.

Contact with the editorial office

This author submitted this manuscript using his/her account in EVISE.

We understand that this Corresponding Author is the sole contact for the Editorial process (including EVISE and direct communications with the office). He/she is responsible for communicating with the other authors about progress, submissions of revisions and final approval of proofs.

We confirm that the email address shown below is accessible by the Corresponding Author, is the address to which Corresponding Author's EVISE account is linked, and has been configured to accept email from the editorial office of American Journal of Ophthalmology Case Reports.

Declaration of competing interest

Potential conflict of interest exists:
No conflict of interest exists.

Acknowledgements

This work is financed by Agence Nationale de la Recherche

(BIORESORB ANR-21-CE18-0012-01). Y. Z. is granted by China Scholarship Council (N° CSC 202106340022).

References

[1] S. Mendis, P. Puska, B. Norrving, Global Atlas on Cardiovascular Disease Prevention and Control, World Health Organization. World Stroke Organization, Copenhagen, 2011.

[2] M. Vaduganathan, G.A. Mensah, J.V. Turco, V. Fuster, G.A. Roth, The global burden of cardiovascular diseases and risk: a compass for future health, J. Am. Coll. Cardiol. 80 (25) (2022) 2361–2371.

[3] M.A. Zain, R.T. Jamil, W.J. Siddiqui, Neointimal hyperplasia, in: StatPearls, StatPearls Publishing, Treasure Island (FL), 2022.

[4] Y. Ruan, R. Yang, Relationship between stent fracture and stent thrombosis, Nat. Rev. Cardiol. 17 (1) (2020), 64-64.

[5] R.J. Guillory, P.K. Bowen, S.P. Hopkins, E.R. Shearier, E.J. Earley, A.A. Gillette, E. Aghion, M. Bocks, J.W. Drelich, J. Goldman, Corrosion characteristics dictate the long-term inflammatory profile of degradable zinc arterial implants, ACS Biomater. Sci. Eng. 2 (12) (2016) 2355–2364.

[6] H. Tamai, K. Igaki, E. Kyo, K. Kosuga, A. Kawashima, S. Matsui, H. Komori, T. Tsuji, S. Motohara, H. Uehata, Initial and 6-month results of biodegradable Poly-l-Lactic acid coronary stents in humans, Circulation 102 (4) (2000) 399–404.

[7] P.W. Serruys, A.T. Ong, J.J. Piek, F.-J. Neumann, W.J. van der Giessen, M. Wiemer, A. Zeiher, E. Grube, J. Haase, L. Thuesen, A Randomized Comparison of a Durable Polymer Everolimus-Eluting Stent with a Bare Metal Coronary Stent: the SPIRIT First Trial. The Unrestricted Use of Paclitaxel-Eluting Stents and Sirolimus-Eluting Stents in the Rotterdam T-SEARCH and RESEARCH Registries: Studies on Efficacy, Safety, Stent Thrombosis, 2005, p. 267.

[8] R. Erbel, C. Di Mario, J. Bartunek, J. Bonnier, B. de Bruyne, F.R. Eberli, P. Erne, M. Haude, B. Heublein, M. Horrigan, C. Ilsley, D. Böse, J. Koolen, T.F. Lüscher, N. Weissman, R. Waksman, Temporary scaffolding of coronary arteries with bioabsorbable magnesium stents: a prospective, non-randomised multicentre trial, Lancet 369 (9576) (2007) 1869–1875.

[9] H. Yang, B. Jia, Z. Zhang, X. Qu, G. Li, W. Lin, D. Zhu, K. Dai, Y. Zheng, Alloying design of biodegradable zinc as promising bone implants for load-bearing applications, Nat. Commun. 11 (1) (2020) 401.

[10] P.K. Bowen, J. Drelich, J. Goldman, Zinc exhibits ideal physiological corrosion behavior for bioabsorbable stents, Adv. Mater. 25 (18) (2013) 2577–2582.

[11] E. Mostaed, M. Sikora-Jasinska, J.W. Drelich, M. Vedani, Zinc-based alloys for degradable vascular stent applications, Acta Biomater. 71 (2018) 1–23.

[12] H. Yang, C. Wang, C. Liu, H. Chen, Y. Wu, J. Han, Z. Jia, W. Lin, D. Zhang, W. Li, W. Yuan, H. Guo, H. Li, G. Yang, D. Kong, D. Zhu, K. Takashima, L. Ruan, J. Nie, X. Li, Y. Zheng, Evolution of the degradation mechanism of pure zinc stent in the one-year study of rabbit abdominal aorta model, Biomaterials 145 (2017) 92–105.

[13] Z. Zhang, B. Jia, H. Yang, Y. Han, Q. Wu, K. Dai, Y. Zheng, Biodegradable ZnLiCa ternary alloys for critical-sized bone defect regeneration at load-bearing sites: in vitro and in vivo studies, Bioact. Mater. 6 (11) (2021) 3999–4013.

[14] G. Bao, Q. Fan, D. Ge, K. Wang, M. Sun, Z. Zhang, H. Guo, H. Yang, B. He, Y. Zheng, In vitro and in vivo studies to evaluate the feasibility of Zn-0.1Li and Zn-0.8Mg application in the uterine cavity microenvironment compared to pure zinc, Acta Biomater. 123 (2021) 393–406.

[15] H. Yang, X. Qu, M. Wang, H. Cheng, B. Jia, J. Nie, K. Dai, Y. Zheng, Zn-0.4Li alloy shows great potential for the fixation and healing of bone fractures at load-bearing sites, Chem. Eng. J. 417 (2021), 129317.

[16] Z. Zhang, B. Jia, H. Yang, Y. Han, Q. Wu, K. Dai, Y. Zheng, Zn0.8Li0.1Sr - a biodegradable metal with high mechanical strength comparable to pure Ti for the treatment of osteoporotic bone fractures: in vitro and in vivo studies, Biomaterials 275 (2021), 120905.

[17] W. Lin, L. Qin, H. Qi, D. Zhang, G. Zhang, R. Gao, H. Qiu, Y. Xia, P. Cao, X. Wang, W. Zheng, Long-term in vivo corrosion behavior, biocompatibility and bioresorption mechanism of a bioresorbable nitrided iron scaffold, Acta Biomater. 54 (2017) 454–468.

[18] H. Hermawan, A. Purnama, D. Dube, J. Couet, D. Mantovani, Fe–Mn alloys for metallic biodegradable stents: degradation and cell viability studies, Acta Biomater. 6 (5) (2010) 1852–1860.

[19] M. Schinhammer, A.C. Hänzi, J.F. Löffler, P.J. Uggowitzer, Design strategy for biodegradable Fe-based alloys for medical applications, Acta Biomater. 6 (5) (2010) 1705–1713.

[20] J. Cheng, T. Huang, Y.F. Zheng, Relatively uniform and accelerated degradation of pure iron coated with micro-patterned Au disc arrays, Mater. Sci. Eng. C 48 (2015) 679–687.

[21] T. Huang, Y. Zheng, Uniform and accelerated degradation of pure iron patterned by Pt disc arrays, Sci. Rep. 6 (1) (2016), 23627.

[22] Y. Qi, H. Qi, Y. He, W. Lin, P. Li, L. Qin, Y. Hu, L. Chen, Q. Liu, H. Sun, Q. Liu, G. Zhang, S. Cui, J. Hu, L. Yu, D. Zhang, J. Ding, Strategy of metal–polymer composite stent to accelerate biodegradation of iron-based biomaterials, ACS Appl. Mater. Interfaces 10 (1) (2018) 182–192.

[23] E. Scarcello, D. Lison, Are Fe-based stenting materials biocompatible? A critical review of In vitro and in vivo studies, J. Funct. Biomater. 11 (1) (2020).

[24] A.A. Oliver, M. Sikora-Jasinska, A.G. Demir, R.J. Guillory, Recent advances and directions in the development of bioresorbable metallic cardiovascular stents: insights from recent human and in vivo studies, Acta Biomater. 127 (2021) 1–23.

[25] D.J. Dries, J.J. Marini, in: R.B. Claudio Ronco, John A. Kellum (Eds.), Critical Care Nephrology, second ed., W.B. Saunders, 2009, pp. 22–31.

[26] Z. Zhen, T.-f. Xi, Y.-f. Zheng, A review on in vitro corrosion performance test of biodegradable metallic materials, Trans. Nonferrous Metals Soc. China 23 (8) (2013) 2283–2293.

[27] D. Mei, S.V. Lamaka, X. Lu, M.L. Zheludkevich, Selecting medium for corrosion testing of bioabsorbable magnesium and other metals – a critical review, Corrosion Sci. 171 (2020), 108722.

[28] R. Oriňaková, R. Gorejová, Z.O. Králová, A. Oriňak, I. Shepa, J. Hovancová, A. Kovalčíková, Z.L. Bujňáková, N. Király, M. Kaňuchová, M. Baláž, M. Strečková, M. Kupková, M. Hrubovčáková, F. Kaľavský, M. Oriňak, Influence of albumin interaction on corrosion resistance of sintered iron biomaterials with polyethyleneimine coating, Appl. Surf. Sci. 509 (2020), 145379.

[29] E. Scarcello, I. Lobysheva, C. Bouzin, P.J. Jacques, D. Lison, C. Dessy, Endothelial dysfunction induced by hydroxyl radicals – the hidden face of biodegradable Fe-based materials for coronary stents, Mater. Sci. Eng. C 112 (2020), 110938.

[30] C. Abe, T. Miyazawa, T. Miyazawa, Current Use of Fenton Reaction in Drugs and Food *Molecules*, 2022, p. 5451.

[31] H.J.H. Fenton, Oxidation of tartaric acid in presence of iron, J. Chem. Soc. Trans. 65 (0) (1894) 899–910.

[32] L.M. Bystrom, M.L. Guzman, S. Rivella, Iron and reactive oxygen species: friends or foes of cancer cells? Antioxidants Redox Signal. 20 (12) (2012) 1917–1924.

[33] ASTM G102-89(2015)E1, in: Standard Practice for Calculation of Corrosion Rates and Related Information from Electrochemical Measurements, ASTM Book of Standards, 2015.

[34] ASTM G31-72(2004), in: Standard Practice for Laboratory Immersion Corrosion Testing of Metals, ASTM Book of Standards, 2004.

[35] M. Moravej, F. Prima, M. Fiset, D. Mantovani, Electroformed iron as new biomaterial for degradable stents: development process and structure–properties relationship, Acta Biomater. 6 (5) (2010) 1726–1735.

[36] B. Liu, Y.F. Zheng, Effects of alloying elements (Mn, Co, Al, W, Sn, B, C and S) on biodegradability and in vitro biocompatibility of pure iron, Acta Biomater. 7 (3) (2011) 1407–1420.

[37] M. Dehestani, E. Adolfsson, L.A. Stanciu, Mechanical properties and corrosion behavior of powder metallurgy iron-hydroxyapatite composites for biodegradable implant applications, Mater. Des. 109 (2016) 556–569.

[38] J. Cheng, Y. Zheng, In vitro study on newly designed biodegradable Fe-X composites (X = W, CNT) prepared by spark plasma sintering, J. Biomed. Mater. Res. B Appl. Biomater. 101B (4) (2013) 485–497.

[39] P. Sharma, P.M. Pandey, Corrosion behaviour of the porous iron scaffold in simulated body fluid for biodegradable implant application, Mater. Sci. Eng. C 99 (2019) 838–852.

[40] Y. Li, H. Jahr, K. Lietaert, P. Pavanram, A. Yilmaz, L.I. Fockaert, M.A. Leeflang, B. Pouran, Y. Gonzalez-Garcia, H. Weinans, J.M.C. Mol, J. Zhou, A.A. Zadpoor, Additively manufactured biodegradable porous iron, Acta Biomater. 77 (2018) 380–393.

[41] S. Bagherifard, M.F. Molla, D. Kajanek, R. Donnini, B. Hadzima, M. Guagliano, Accelerated biodegradation and improved mechanical performance of pure iron through surface grain refinement, Acta Biomater. 98 (2019) 88–102.

[42] J. Cheng, T. Huang, Y.F. Zheng, Microstructure, mechanical property, biodegradation behavior, and biocompatibility of biodegradable Fe–Fe2O3 composites, J. Biomed. Mater. Res. 102 (7) (2014) 2277–2287.

[43] L. Yang, E. Zhang, Biocorrosion behavior of magnesium alloy in different simulated fluids for biomedical application, Mater. Sci. Eng. C 29 (5) (2009) 1691–1696.

[44] J. Frattolin, R. Barua, H. Aydin, S. Rajagopalan, L. Gottellini, R. Leask, S. Yue, D. Frost, O.F. Bertrand, R. Mongrain, Development of a novel biodegradable metallic stent based on microgalvanic effect, Ann. Biomed. Eng. 44 (2) (2016) 404–418.

[45] M.-K. Lee, H. Lee, C. Park, I.-G. Kang, J. Kim, H.-E. Kim, H.-D. Jung, T.-S. Jang, Accelerated biodegradation of iron-based implants via tantalum-implanted surface nanostructures, Bioact. Mater. 9 (2022) 239–250.

[46] N.E. Putra, M.A. Leeflang, M. Minneboo, P. Taheri, L.E. Fratila-Apachitei, J.M. C. Mol, J. Zhou, A.A. Zadpoor, Extrusion-based 3D printed biodegradable porous iron, Acta Biomater. 121 (2021) 741–756.

[47] Č. Donik, A. Kocijan, I. Paulin, M. Hočevar, P. Gregorčič, M. Godec, Improved biodegradability of Fe–Mn alloy after modification of surface chemistry and topography by a laser ablation, Appl. Surf. Sci. 453 (2018) 383–393.

[48] T. Huang, J. Cheng, D. Bian, Y. Zheng, Fe–Au and Fe–Ag composites as candidates for biodegradable stent materials, J. Biomed. Mater. Res. B Appl. Biomater. 104 (2) (2016) 225–240.

[49] H. Wang, Y. Zheng, Y. Li, C. Jiang, Improvement of in vitro corrosion and cytocompatibility of biodegradable Fe surface modified by Zn ion implantation, Appl. Surf. Sci. 403 (2017) 168–176.

[50] T. Huang, J. Cheng, Y.F. Zheng, In vitro degradation and biocompatibility of Fe–Pd and Fe–Pt composites fabricated by spark plasma sintering, Mater. Sci. Eng. C 35 (2014) 43–53.

[51] Y. Qi, X. Li, Y. He, D. Zhang, J. Ding, Mechanism of acceleration of iron corrosion by a polylactide coating, ACS Appl. Mater. Interfaces 11 (1) (2019) 202–218.

[52] B. Wegener, A. Sichler, S. Milz, C. Sprecher, K. Pieper, W. Hermanns, V. Jansson, B. Nies, B. Kieback, P.E. Müller, V. Wegener, P. Quadbeck, Development of a novel biodegradable porous iron-based implant for bone replacement, Sci. Rep. 10 (1) (2020) 9141.

[53] P. Sharma, P.M. Pandey, A novel manufacturing route for the fabrication of topologically-ordered open-cell porous iron scaffold, Mater. Lett. 222 (2018) 160–163.

[54] P. Sharma, K.G. Jain, P.M. Pandey, S. Mohanty, In vitro degradation behaviour, cytocompatibility and hemocompatibility of topologically ordered porous iron scaffold prepared using 3D printing and pressureless microwave sintering, Mater. Sci. Eng. C 106 (2020), 110247.

[55] C.S. Obayi, R. Tolouei, A. Mostavan, C. Paternoster, S. Turgeon, B.A. Okorie, D. O. Obikwelu, D. Mantovani, Effect of grain sizes on mechanical properties and biodegradation behavior of pure iron for cardiovascular stent application, Biomatter 6 (1) (2016), e959874.

[56] V.P.M. Rabeeh, T. Hanas, Progress in manufacturing and processing of degradable Fe-based implants: a review, Progr. Biomater. 11 (2) (2022) 163–191.

[57] O.V. Rybalchenko, N.Y. Anisimova, M.V. Kiselevsky, G.V. Rybalchenko, N. S. Martynenko, N.R. Bochvar, N.Y. Tabachkova, I.V. Shchetinin, T.V. Shibaeva, S. V. Konushkin, A.A. Tokar, A.G. Raab, S.V. Dobatkin, Effect of equal-channel angular pressing on structure and properties of Fe-Mn-C alloys for biomedical applications, Mater. Today Commun. 30 (2022), 103048.

[58] J. Frattolin, R. Roy, S. Rajagopalan, M. Walsh, S. Yue, O.F. Bertrand, R. Mongrain, A manufacturing and annealing protocol to develop a cold-sprayed Fe-316L stainless steel biodegradable stenting material, Acta Biomater. 99 (2019) 479–494.

[59] G. Mani, M.D. Feldman, D. Patel, C.M. Agrawal, Coronary stents: a materials perspective, Biomaterials 28 (9) (2007) 1689–1710.

[60] Y. Xu, W. Wang, F. Yu, Y. Wang, M. Qi, Y. Zhao, Y. Wang, Effects of pulse frequency and current density on microstructure and properties of biodegradable Fe-Zn alloy, J. Mater. Res. Technol. 18 (2022) 44–58.

[61] M.A. Maruf, M. Noor-A-Alam, W. Haider, I. Shabib, Enhancing controlled and uniform degradation of Fe by incorporating Mg and Zn aimed for bio-degradable material applications, Mater. Chem. Phys. 285 (2022), 126171.

[62] C. Shuai, S. Li, G. Wang, Y. Yang, S. Peng, C. Gao, Strong corrosion induced by carbon nanotubes to accelerate Fe biodegradation, Mater. Sci. Eng. C 104 (2019), 109935.

[63] M.S. Dargusch, J. Venezuela, A. Dehghan-Manshadi, S. Johnston, N. Yang, K. Mardon, C. Lau, R. Allavena, In vivo evaluation of bioabsorbable Fe-35Mn-1Ag: first reports on in vivo hydrogen gas evolution in Fe-based implants, Adv. Healthc. Mater. 10 (2) (2021), 2000667.

[64] Y. Sun, L. Chen, N. Liu, H. Wang, C. Liang, Laser-modified Fe–30Mn surfaces with promoted biodegradability and biocompatibility toward biological applications, J. Mater. Sci. 56 (24) (2021) 13772–13784.

[65] M. Wiesener, K. Peters, A. Taube, A. Keller, K.P. Hoyer, T. Niendorf, G. Grundmeier, Corrosion properties of bioresorbable FeMn-Ag alloys prepared by selective laser melting, Mater. Corros. 68 (10) (2017) 1028–1036.

[66] R.-Y. Liu, R.-G. He, L.-Q. Xu, S.-F. Guo, Design of Fe–Mn–Ag alloys as potential candidates for biodegradable metals, Acta Metall. Sin. 31 (6) (2018) 584–590.

[67] J. Wood, G. Majumdar, Ion implantation, in: Reference Module in Materials Science and Materials Engineering, Elsevier, 2016.

[68] T. Huang, Y. Zheng, Y. Han, Accelerating degradation rate of pure iron by zinc ion implantation, Regen. Biomater. 3 (4) (2016) 205–215.

[69] A.H.M. Yusop, N.M. Daud, H. Nur, M.R.A. Kadir, H. Hermawan, Controlling the degradation kinetics of porous iron by poly(lactic-co-glycolic acid) infiltration for use as temporary medical implants, Sci. Rep. 5 (1) (2015), 11194.

[70] G. Papanikolaou, K. Pantopoulos, Iron metabolism and toxicity, Toxicol. Appl. Pharmacol. 202 (2) (2005) 199–211.

[71] N.S. Fagali, C.A. Grillo, S. Puntarulo, M.A. Fernández Lorenzo de Mele, Cytotoxicity of corrosion products of degradable Fe-based stents: relevance of pH and insoluble products, Colloids Surf. B Biointerfaces 128 (2015) 480–488.

[72] S. Zhu, N. Huang, L. Xu, Y. Zhang, H. Liu, H. Sun, Y. Leng, Biocompatibility of pure iron: in vitro assessment of degradation kinetics and cytotoxicity on endothelial cells, Mater. Sci. Eng. C 29 (5) (2009) 1589–1592.

[73] ISO 10993-5, In Biological Evaluation of Medical Devices — Part 5: Tests for in Vitro Cytotoxicity, 2009.

[74] D.P. Wermuth, T.C. Paim, I. Bertaco, C. Zanatelli, L.I.S. Naasani, M. Slaviero, D. Driemeier, A.C. Tavares, V. Martins, C.F. Escobar, L.A.L. dos Santos, L. Schaeffer, M.R. Wink, Mechanical properties, in vitro and in vivo biocompatibility analysis of pure iron porous implant produced by metal injection molding: a new eco-friendly feedstock from natural rubber (Hevea brasiliensis), Mater. Sci. Eng. C 131 (2021), 112532.

[75] A. Purnama, H. Hermawan, S. Champetier, D. Mantovani, J. Couet, Gene expression profile of mouse fibroblasts exposed to a biodegradable iron alloy for stents, Acta Biomater. 9 (10) (2013) 8746–8753.

[76] N.S. Fagali, C.A. Grillo, S. Puntarulo, M.A. Fernández Lorenzo de Mele, Is there any difference in the biological impact of soluble and insoluble degradation products of iron-containing biomaterials? Colloids Surf. B Biointerfaces 160 (2017) 238–246.

[77] H. Hermawan, D. Dubé, D. Mantovani, Developments in metallic biodegradable stents, Acta Biomater. 6 (5) (2010) 1693–1697.

[78] P.P. Mueller, T. May, A. Perz, H. Hauser, M. Peuster, Control of smooth muscle cell proliferation by ferrous iron, Biomaterials 27 (10) (2006) 2193–2200.

[79] W. Lin, G. Zhang, P. Cao, D. Zhang, Y. Zheng, R. Wu, L. Qin, G. Wang, T. Wen, Cytotoxicity and its test methodology for a bioabsorbable nitrided iron stent, J. Biomed. Mater. Res. B Appl. Biomater. 103 (4) (2015) 764–776.

[80] C. Delattre, D. Velazquez, C. Roques, G. Pavon-Djavid, V. Ollivier, A. Lokajczyk, T. Avramoglou, V. Gueguen, L. Louedec, G. Caligiuri, M. Jandrot-Perrus, C. Boisson-Vidal, D. Letourneur, A. Meddahi-Pelle, In vitro and in vivo evaluation of a dextran-graft-polybutylmethacrylate copolymer coated on CoCr metallic stent, Bioimpacts 9 (1) (2019) 25–36.

[81] M. Mozafari, Chapter 1 - principles of biocompatibility, in: M. Mozafari (Ed.), Handbook of Biomaterials Biocompatibility, Woodhead Publishing, 2020, pp. 3–9.

[82] D.P. Vasconcelos, A.P. Águas, M.A. Barbosa, P. Pelegrín, J.N. Barbosa, The inflammasome in host response to biomaterials: bridging inflammation and tissue regeneration, Acta Biomater. 83 (2019) 1–12.

[83] B. Paul, A. Lode, A.-M. Placht, A. Voß, S. Pilz, U. Wolff, S. Oswald, A. Gebert, M. Gelinsky, J. Hufenbach, Cell–material interactions in direct contact culture of endothelial cells on biodegradable iron-based stents fabricated by laser powder bed fusion and impact of ion release, ACS Appl. Mater. Interfaces 14 (1) (2022) 439–451.

[84] E. Mouzou, C. Paternoster, R. Tolouei, P. Chevallier, C.A. Biffi, A. Tuissi, D. Mantovani, CO_2-rich atmosphere strongly affects the degradation of Fe-21Mn-1C for biodegradable metallic implants, Mater. Lett. 181 (2016) 362–366.

[85] B. Halliwell, O.I. Aruoma, DNA damage by oxygen-derived species its mechanism and measurement in mammalian systems, FEBS (Fed. Eur. Biochem. Soc.) Lett. 281 (1–2) (1991) 9–19.

[86] S. Nemoto, K. Takeda, Z.-X. Yu, J. Ferrans Victor, T. Finkel, Role for mitochondrial oxidants as regulators of cellular metabolism, Mol. Cell Biol. 20 (19) (2000) 7311–7318.

[87] M. Schieber, Navdeep S. Chandel, ROS function in redox signaling and oxidative stress, Curr. Biol. 24 (10) (2014) R453–R462.

[88] J. Xia, H. Si, W. Yao, C. Li, G. Yang, Y. Tian, C. Hao, Research progress on the mechanism of ferroptosis and its clinical application, Exp. Cell Res. 409 (2) (2021), 112932.

[89] H. Zhang, W. Zhang, H. Qiu, G. Zhang, X. Li, H. Qi, J. Guo, J. Qian, X. Shi, X. Gao, D. Shi, D. Zhang, R. Gao, J. Ding, A biodegradable metal-polymer composite stent safe and effective on physiological and serum-containing biomimetic conditions, Adv. Healthc. Mater. 11 (22) (2022), 2201740.

[90] N.S. Fagali, M.A. Madrid, B.T. Pérez Maceda, M.E. López Fernández, R.M. Lozano Puerto, M. Fernández Lorenzo de Mele, Effect of degradation products of iron-bioresorbable implants on the physiological behavior of macrophages in vitro, Metallomics 12 (11) (2020) 1841–1850.

[91] Y. Zhao, J. Feng, H. Yu, W. Lin, X. Li, Y. Tian, M. Zhao, Comparative study on biodegradation of pure iron prepared by microwave sintering and laser melting, Materials 15 (4) (2022) 1604.

[92] R. Wang, J. Lu, J. Yin, H. Chen, H. Liu, F. Xu, T. Zang, R. Xu, C. Li, Y. Wu, Q. Wu, X. Fei, M. Zhu, L. Shen, J. Ge, A TEMPOL and rapamycin loaded nanofiber-covered stent favors endothelialization and mitigates neointimal hyperplasia and local inflammation, Bioact. Mater. 19 (2023) 666–677.

[93] S. Hu, Z. Li, D. Shen, D. Zhu, K. Huang, T. Su, P.-U. Dinh, J. Cores, K. Cheng, Exosome-eluting stents for vascular healing after ischaemic injury, Nat. Biomed. Eng. 5 (10) (2021) 1174–1188.

[94] M. Peuster, P. Wohlsein, M. Brügmann, M. Ehlerding, K. Seidler, C. Fink, H. Brauer, A. Fischer, G. Hausdorf, A novel approach to temporary stenting: degradable cardiovascular stents produced from corrodible metal-results 6-18 months after implantation into New Zealand white rabbits, Heart 86 (5) (2001) 563–569.

[95] C. Wu, H. Qiu, X. Hu, Y. Ruan, Y. Tian, Y. Chu, X. Xu, L. Xu, Y. Tang, R. Gao, Short-term safety and efficacy of the biodegradable iron stent in mini-swine coronary arteries, Chin. Med. J. 126 (24) (2013) 4752–4757.

[96] W.A. Wan Ahmad, T. Nakayoshi, A.S. Mahmood Zuhdi, M.D. Ismail, I. Zainal Abidin, Y. Ino, T. Kubo, T. Akasaka, Y. Fukumoto, T. Ueno, Different vascular healing process between bioabsorbable polymer-coated everolimus-eluting stents versus bioresorbable vascular scaffolds via optical coherence tomography and coronary angioscopy (the enhance study: endothelial healing assessment with novel coronary technology), Heart Ves. 35 (4) (2020) 463–473.

[97] R. Rampat, T. Williams, T. Mayo, M. Mengozzi, P. Ghezzi, D. Hildick-Smith, J. Cockburn, Association between inflammatory biomarkers and neointimal response following elective implantation of the ABSORB bioresorbable vascular scaffold, Coron. Artery Dis. 30 (3) (2019).

[98] E. Scarcello, A. Herpain, M. Tomatis, F. Turci, P.J. Jacques, D. Lison, Hydroxyl radicals and oxidative stress: the dark side of Fe corrosion, Colloids Surf. B Biointerfaces 185 (2020), 110542.

[99] Q. Feng, D. Zhang, C. Xin, X. Liu, W. Lin, W. Zhang, S. Chen, K. Sun, Characterization and in vivo evaluation of a bio-corrodible nitrided iron stent, J. Mater. Sci. Mater. Med. 24 (3) (2013) 713–724.

[100] D. Qiu, Y. Deng, Y. Wen, J. Yin, J. Feng, J. Huang, M. Song, G. Zhang, C. Chen, J. Xia, Iron corroded granules inhibiting vascular smooth muscle cell proliferation, Mater. Today Bio. 16 (2022), 100420.

[101] X. Li, W. Zhang, W. Lin, H. Qiu, Y. Qi, X. Ma, H. Qi, Y. He, H. Zhang, J. Qian, G. Zhang, R. Gao, D. Zhang, J. Ding, Long-term efficacy of biodegradable metal–polymer composite stents after the first and the second implantations into porcine coronary arteries, ACS Appl. Mater. Interfaces 12 (13) (2020) 15703–15715.

[102] W. Lin, H. Zhang, W. Zhang, H. Qi, G. Zhang, J. Qian, X. Li, L. Qin, H. Li, X. Wang, H. Qiu, X. Shi, W. Zheng, D. Zhang, R. Gao, J. Ding, In vivo degradation and endothelialization of an iron bioresorbable scaffold, Bioact. Mater. 6 (4) (2021) 1028–1039.

[103] D. Qiu, J. Yin, Y. Wen, J. Huang, T. Lei, C. Chen, J. Xia, Diabetes-induced iron stent degradation but preventing re-endothelialization after implantation, Mater. Des. 229 (2023), 111930.

[104] M. Peuster, C. Hesse, T. Schloo, C. Fink, P. Beerbaum, C. von Schnakenburg, Long-term biocompatibility of a corrodible peripheral iron stent in the porcine descending aorta, Biomaterials 27 (28) (2006) 4955–4962.

[105] R. Waksman, R. Pakala, R. Baffour, R. Seabron, D. Hellinga, F.O. Tio, Short-term effects of biocorrodible iron stents in porcine coronary arteries, J. Intervent. Cardiol. 21 (1) (2008) 15–20.
[106] C. Shuai, S. Li, W. Yang, Y. Yang, Y. Deng, C. Gao, MnO2 catalysis of oxygen reduction to accelerate the degradation of Fe-C composites for biomedical applications, Corrosion Sci. 170 (2020), 108679.
[107] S. Li, J. Ren, X. Li, X. Wang, A. Cai, Y. Ding, Y. Yang, Combined effects of rapid dissolution and micro-acidification accelerated Fe biodegradation for orthopedic applications, Corrosion Sci. 216 (2023), 111067.
[108] Y. Yang, G. Cai, M. Yang, D. Wang, S. Peng, Z. Liu, C. Shuai, Laser additively manufactured iron-based biocomposite: microstructure, degradation, and in vitro cell behavior, Front. Bioeng. Biotechnol. 9 (2021).

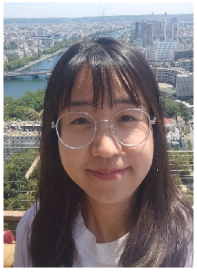

Yang Zhang is a PhD candidate, hosted bylaboratory of pharmacological and toxicological chemistry and biochemistry (LCBPT, CNRS UMR 8601, Université Paris Cite) and laboratory for vascular translation science (LVTS, INSERM UMRS1148), majored in chemistry and physics. Her PhD project focuses on surface chemistry and biocompatibility assessment for cardiovascular implants. ORCID 0009-0008-3486-2801.

Charles Roux is MD, MsC specialized in interventional Radiology with particular interest in endovascular treatments. He is PhD candidate in Institut XLIM CNRS UMR 7252 laboratory and head of Pitié-Salpètrière interventional radiology since May 2022. His research interests focus on new endovascular device and in portal hypertension endovascular treatment. ORCID 0000-0002-9584-3048.

Aymeric Rouchaud, MD, PhD and full professor of Interventional Neuroradiology, President research of the ESMINT Society (European Society of Minimally Invasive Neurological Therapy). Aymeric Rouchaud is director of the Bio-Health Group in XLIM CNRS UMR7252 laboratory. His team is invested in preclinical research for endovascular therapy and microvascular navigation in animals with a special focus on biological optimization of endovascular treatments with stents. His experiments are performed within the EMIS experimental platform he co-chairs (https://emis-research.com) ORCID: 0000-0003-0902-3375. Personal page: https://scholar.google.com/citations?hl=en&user=aYaazZYAAAAJ

Anne Meddahi-Pellé: Professor of Universities, Sorbonne Paris Nord University, Inserm UMR 1148, LVTS. Anne Pellé was appointed professor at the University of Orleans in 2003, then at the University of Versailles Saint Quentin, in 2009. Currently at the University Sorbonne Paris Nord, she was vice-president in charge of research and doctoral studies (2016–2020) and is currently vice-president in charge of the academic council. She has been responsible for numerous training courses (masters, bachelors, DUT) and has exercised numerous institutional responsibilities. Within the LVTS team 3, her research work is at the interface between biology, physiology, medicine and engineering. The objectives are the development and preclinical validation of implantable medical devices. This interdisciplinary work has allowed her to train many students from different backgrounds (engineers, physicians, pharmacists, biologists) in this conceptual approach. This research has led to the production of publications and to the filing and valorization of patents. ORCID 0000-0002-4868-2093.

Virginie Gueguen obtained her PhD from Ecole Nationale Supérieure des Arts et Métiers in 1992 in Mechanics and Materials. Since 1994, she is assistant professor. From 1994 to 2002, she worked in the polymer field applied to textile industry in Gemtex laboratory in Ecole Nationale Supérieure des Arts et Industries Textiles (Roubaix). She joined Université Paris 13 in 2002, and LVTS Laboratory in 2008. Her research field covers drug delivery systems from elaboration to physico chemical characterizations. ORCID 0000-0003-2500-0747.

Claire Mangeney obtained her PhD from Paris Diderot University in 2000 in conducting polymer chemistry. Since 2016, she is full professor in LCBPT lab in Université Paris Cité. Her research interest is at the interface of surface chemistry, nanotechnology and biology. Her primary goal is to develop hybrid nanomaterials for biological-related applications. She has developed over the last decade original chemical strategies to attach polymers (brushes, imprinted and smart polymers, hydrogels) on planar and micro/nano-structured surfaces using diazonium salts as a new generation of coupling agents. ORCID 0000-0002-9817-3262.

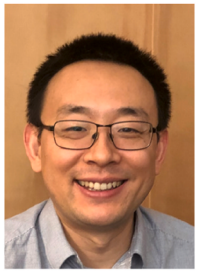

Fan Sun received his PhD degree on metallurgy from INSA-Rennes France in 2010. He is a permanent researcher at Métallurgie Structurale team of Chimie-Paristech, PSL unviersity since 2017 with Habilitation à diriger des recherches (HDR). His research focus on metallic biomaterials, such as new Ti alloys, Zr alloys, Fe alloys, Zn alloys and conventional NiTi and CoCr alloys, for cardiovascular implant applications. ORCID 0000-0002-4669–121×. Email: fan.sun@chimieparistech.psl.eu Personal page: https://scholar.google.com/citations?user=q3q8bLMAAAAJ&hl=en

Graciela Pavon-Djavid obtained her PhD from Université Sorbonne Paris Nord in 1992 in chemistry and in 2013 her Accreditation to Supervise Research in Science (HDR) in physiology. She is research engineer at U1148 INSERM unit lab. Her research interest focuses on the development of new strategies in cardiovascular bioengineering and on the development of drug delivery systems. She has extensive experience in the field of biocompatibility assessment of medical devices *in vitro* and *in vivo* and on antioxidants and oxidative stress specifically related to biomaterials. ORCID 0000-0001-5819-1071. Personal page: https://scholar.google.com/citations?user=OAGHTqAAAAAJ&hl=fr Email: graciela.pavon@univ-paris13.fr

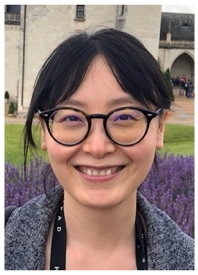

Yun Luo received her PhD degree on materials chemistry from INSA-Rennes France in 2012. She is tenured CNRS research scientist (CRCN) since 2019 and leading Nano Bio Spectroscopy team in LCBPT lab (CNRS UMR 8601) at Université Paris Cité since 2022. Her research interests focus on surface chemistry and surface functionalization of biomaterials for multimodal bioimaging, multifunctional drug delivery system, cancer theranostics and implantable medical devices. She is co-authored of over 40 peer-reviewed publications and received 2 grants from French National Research Agency (ANR) since2021. ORCID 0000-0002-9515-0460. Email: yun.luo@u-paris.fr Personal page https://scholar.google.fr/citations?user=wWChhMUAAAAJ&hl=fr.